WHEN DO RANKINGS BEAT SIGNS? GRADIENT DIRECTION RECOVERY UNDER EVEN NUISANCE

Anonymous authors
Paper under double-blind review

ABSTRACT

Can ranking a batch of antipodal query pairs recover a gradient direction with fewer evaluations than using within-pair signs alone? We study fixed-center recovery in d dimensions for a linear signal plus an unknown differentiable even nuisance, counting function evaluations and feedback rounds separately. Shared pair offsets create an information hierarchy: Mirror retains within-pair signs, Reverse couples reversed cross-pair orders to cancel offsets, and Full enforces all ranking inequalities. Relative shell variation is the nuisance range over the query sphere normalized by the linear-signal scale. When it is at most $c\varepsilon/\sqrt{d}$, Reverse localizes every consistent direction to angular accuracy ε using $\widetilde{O}(d + \sqrt{d/\varepsilon})$ evaluations in one round at fixed confidence, without a variation bound supplied to the decoder. This matches a lower bound up to logarithmic factors, versus the $\Theta(d/\varepsilon)$ one-round sign-only minimax cost on the same class. Over well-conditioned positive-definite quadratics with no common relative-curvature bound, the R-round minimax cost is instead $\Theta(dR(\varepsilon^{-1/R} - 1))$, even with cumulative rankings. We extend validity beyond exact evenness under supplied error bounds. Matched-endpoint experiments certify information beyond signs and short cycles. On two ridge tasks under joint evaluation and round caps, short-cycle recovery attains lower terminal mean gaps than the tested batch-capable controls. An additional optimization benefit from fitting the complete ranking remains unestablished.

1 INTRODUCTION

When numerical objective values are unavailable to the optimizer, comparisons can still guide optimization by estimating a local gradient direction (Cai et al., 2022; Zhang & Ying, 2025; Ren et al., 2026; Wang et al., 2026). A ranking interface can return the order of a batch of evaluated points, allowing each point to participate in many comparisons (Tang et al., 2024). Batching is especially relevant when queries can be issued in parallel but feedback rounds are limited (Saha et al., 2024). Function evaluations and feedback rounds are different resources. A larger batch uses more evaluations, whereas adapting the next batch requires another synchronization.

Consider the antipodal batch in Figure 1(a), built from symmetric two-point queries around a fixed recovery center (Lobanov et al., 2024; Saha et al., 2025). Keeping only within-pair signs discards cross-pair orders supplied by a complete ranking without additional function evaluations. Yet unknown nonlinear contributions can alter these orders, and comparisons sharing endpoints need not be independent (Tang et al., 2024). Counting the extra comparisons therefore does not establish a recovery advantage. Tao et al. (2026) establish optimal comparison complexity for gradient-direction estimation using adaptive pairwise queries, given a smoothness constant and a positive gradient-norm lower bound. This adaptive bound does not by itself quantify the benefit of cross-pair orders when all query points are chosen before feedback. We therefore ask: *when can a ranked antipodal batch recover the gradient direction with fewer evaluations than within-pair signs alone, under the same one-round feedback constraint?*

To isolate this question, translate the recovery center to zero and consider

$$f(x) = b + g^\top x + E(x), \qquad x \in \mathbb{R}^d, \qquad g \neq 0, \qquad E(-x) = E(x),$$

where E is an unknown differentiable even nuisance. This includes every quadratic objective at a nonstationary center, without assuming known curvature. Differentiability and evenness give

Reviewers: please read the Reviewer Guidelines (iclr.cc/Conferences/2027/ReviewerGuidelines) and the AI Policy for Reviewers (iclr.cc/Conferences/2027/AIPolicyForReviewers). If you used AI to expand, edit, or polish your review, please provide the input text to the LLM. Better still, consider skipping the LLM and submitting your original text: we, and the authors, are much more interested in your unedited thoughts than in what an LLM has to say. AI-assisted or not, you are putting your name and reputation behind your review: LLM-generated falsehoods, hallucinations or misrepresentations are subject to disciplinary action, which may include desk-rejecting all papers you have authored.

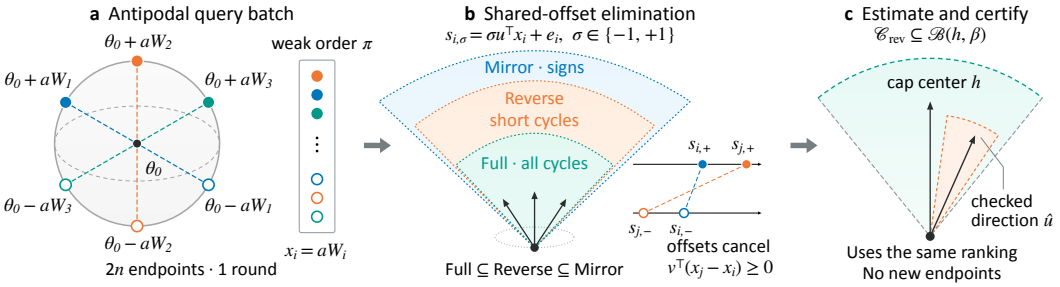

Figure 1: Direction information from a ranked batch. (a) n antipodal pairs require $2n$ function evaluations and one feedback round. (b) Shared-offset elimination gives nested Mirror, Reverse, and Full sets. (c) The same ranking supports a feasibility-checked direction and an optional cap enclosing Reverse and hence Full. Sets are schematic.

$\nabla E(0) = 0$, so $u = g/\|g\|$ is the unit gradient direction. Antipodal points share an offset: $f(x) - f(-x) = 2g^\top x$, so within-pair comparisons reveal exact projection signs.

Cross-pair orders, however, mix differences in the linear signal and the nuisance. Even noiseless orders need not exclude the alternative directions allowed by signs. Nor does an accurate estimate alone establish an information gain: other directions can remain consistent. The challenge is to quantify what the whole batch rules out.

We address this challenge through the three nested direction sets in Figure 1(b). *Mirror* retains within-pair signs, while *Reverse* adds short-cycle constraints from reversed cross-pair orders, cancelling shared offsets without estimating them. *Full* enforces all ranking inequalities with one unrestricted offset per physical pair. Longer cycles can rule out directions that survive every reverse-order constraint. All three contain u under the even-nuisance model. Moving inward in the figure thus means ruling out more directions using the same observations, not acquiring more data. Once the entire set lies within angle ε of u, every estimate in it is ε-accurate, regardless of how it is selected.

The relevant nuisance scale is variation across the query sphere, not its absolute magnitude. We call the range of E on a radius-a sphere divided by $a\|g\|$ the *relative shell variation* τ_a. Isotropic quadratic curvature contributes zero variation, however large its magnitude. With independent uniform query directions, $\tau_a \leq c\varepsilon/\sqrt{d}$ for sufficiently small universal c suffices for Reverse to localize every consistent direction within angle ε of u at a nearly optimal one-round evaluation cost. This condition concerns the actual nuisance. The decoder receives no variation bound, and candidate offsets remain unrestricted. Yet rankings have no minimax evaluation advantage over signs on well-conditioned positive-definite quadratics with no common relative-curvature bound, even with adaptive radii and cumulative rankings.

Finally, Figure 1(c) separates a feasibility-checked direction from an optional cap bounding the remaining uncertainty, with no new endpoints or rounds. Fitting and certification incur separate computational costs. We test information gain separately from optimization under joint evaluation and round caps. A smaller direction set need not yield better task progress.

Our contributions are as follows.

1. We characterize the Mirror–Reverse–Full information hierarchy, showing that longer cycles can exclude directions allowed by all short cycles. We also extend validity beyond exact evenness under supplied error bounds (Sections 2 and 3.3).
2. We prove a nearly optimal $\widetilde{O}(d + \sqrt{d/\varepsilon})$ one-round evaluation bound for whole-cell recovery at fixed confidence, versus $\Theta(d/\varepsilon)$ for signs on the same small-variation class, and a tight endpoint–round tradeoff over the unbounded-scale quadratic class (Theorems 2 and 3).
3. We certify information gains beyond signs and short cycles on matched endpoints, including under higher-rank anisotropy. On two ridge tasks under joint evaluation and sixteen-round caps, Reverse attains lower terminal mean gaps than tested batch-capable controls. Full's additional optimization benefit over Reverse remains unestablished (Section 4).

2 THE MIRROR–REVERSE–FULL INFORMATION HIERARCHY

Problem and resources. Translate the fixed recovery center to zero and write

$$f(x) = b + g^\top x + E(x), \qquad g \neq 0, \qquad E(-x) = E(x). \tag{1}$$

Since E is differentiable and even, $\nabla E(0) = 0$. The target is therefore the unit gradient direction $u = g/\|g\| \in \mathbb{S}^{d-1}$. Let $\mathcal{B}(h, \beta)$ denote the closed cap of unit directions within angle β of h, measured in radians.

A batch is chosen before its feedback arrives. A *batch oracle* ranks the new endpoints; a *cumulative oracle* ranks all endpoints evaluated so far. Both return weak orders, allowing ties. Each endpoint costs one function evaluation (FE), including antipodes, initialization, and repeated evaluations. A round is one feedback synchronization, not a count of comparisons or annotation effort. Sorting, fitting, and certification are separate computational costs. Minimax statements allow measurable query and output rules with independent private randomness and impose hard budgets of N endpoints and R rounds on every history. They require

$$\mathbb{P}\{\mathrm{angle}(\widehat{u}, u) \leq \varepsilon\} \geq 3/4 \quad \text{for every fixed instance.} \tag{2}$$

Upper constructions use batch rankings; lower bounds allow the stronger cumulative oracle.

Observable offset cancellation. For queries $\pm x_i$, subtracting a common constant and dividing by $\|g\| > 0$ gives latent scores

$$s_{i,\sigma} = \sigma u^\top x_i + e_i, \qquad \sigma \in \{-1, +1\}, \qquad e_i = E(x_i)/\|g\|. \tag{3}$$

The decoder observes only their order π, not $\|g\|$ or the offsets. Within a pair, the offset cancels and the order reveals $\mathrm{sign}(u^\top x_i)$. Across pairs, suppose $s_{j,+} > s_{i,+}$ while $s_{j,-} < s_{i,-}$. Any candidate gradient v and offsets z explaining these orders must satisfy

$$\begin{aligned} &v^\top(x_j - x_i) + (z_j - z_i) \geq 0, \\ &v^\top(x_j - x_i) - (z_j - z_i) \geq 0 \end{aligned} \quad \Longrightarrow \quad v^\top(x_j - x_i) \geq 0. \tag{4}$$

Adding the inequalities removes the offset difference without requiring equal or estimated offsets. Reorienting either pair gives the other signed relations.

Three nested direction sets. Full retains every ranking inequality with one unrestricted offset per physical pair:

$$\begin{aligned} K(X, \pi) &= \{(v, z) : \sigma v^\top x_i + z_i \leq \zeta v^\top x_j + z_j \text{ if } (i, \sigma) \preceq_\pi (j, \zeta)\}, \\ \mathcal{C}(X, \pi) &= \mathrm{proj}_v K(X, \pi) \cap \mathbb{S}^{d-1}. \end{aligned} \tag{5}$$

Thus $\mathcal{C}$ is the closed ranking-consistency set, a version space of directions with unrestricted pair offsets (Mitchell, 1982). Strict observations are relaxed to weak candidate inequalities. Observed ties impose both inequalities. Adjacent-order inequalities suffice. Repeated physical pairs share one offset. A common additive offset changes no order, so one offset can be fixed. On one shell $x_i = aW_i$, rescaling gives $\mathcal{C}(W, \pi)$. Across shells, retain physical coordinates and the same gradient. Mirror keeps within-pair signs; Reverse adds all signed relations from Equation (4).

Proposition 1 (Validity and observable elimination)**.** *For every differentiable even nuisance and its observed ranking,*

$$u \in \mathcal{C}(X, \pi) \subseteq \mathcal{C}_{\mathrm{rev}}(X, \pi) \subseteq \mathcal{C}_{\mathrm{mirror}}(X, \pi). \tag{6}$$

For fixed v, Full's ranking inequalities are difference constraints in z, feasible exactly when every directed cycle has nonnegative weight. Mirror signs arise from self-loops, and reverse orders from two-edge cycles. Full retains all cycles.

Each order bounds an offset difference, represented by a directed edge between pairs. Cycle sums cancel the offsets. Without a negative cycle, shortest-path potentials satisfy the constraints (Cormen et al., 2001). The actual offsets witness validity (Appendix A).

Longer cycles can add information even in three dimensions. For the three coordinate vectors, consider

$$s_{2,-} < s_{1,-} < s_{1,+} < s_{3,-} < s_{3,+} < s_{2,+}.$$

Reverse requires $v_1, v_3 \geq 0$ and $v_2 \geq \max\{v_1, v_3\}$. Full additionally requires $v_2 \geq v_1 + v_3$. Pair 2's interval contains the disjoint intervals of pairs 1 and 3, whose widths are $2v_1$ and $2v_3$. A quadratic realization and a separating candidate appear in Appendix A.2.

Decoding and certification. Submit $N = 2n$ endpoints $\theta_0 \pm aW_i$ with independent uniform W_i in one batch. For strict spanning designs, a bounded-section analytic-center fit proposes a direction. The returned unit direction is checked for feasibility (Appendices F.3 and F.4). Full uses $2n - 1$ adjacent-order rows and $d + n - 1$ variables to enforce all cycles without enumeration. Reverse uses d variables. Optional residual-checked caps enclose Reverse and hence Full without computing Full's exact projection or requiring new endpoints or rounds (Appendices F and K). The whole-cell guarantees apply to every consistent selector, regardless of this numerical choice (Appendix A.3).

3 When Rankings Beat Signs

3.1 Small shell variation enables a ranking gain

Define the shell variation $\Omega_a(E)$ and its relative scale τ_a:

$$\Omega_a(E) = \sup_{\|w\|=\|z\|=1} |E(aw) - E(az)|, \qquad \tau_a = \frac{\Omega_a(E)}{a\,\|g\|}. \tag{7}$$

Write $\tau = \tau_a$ on a fixed shell. For $E(x) = x^\top Hx/2$, $\tau_a = a(\lambda_{\max}(H) - \lambda_{\min}(H))/(2\,\|g\|)$. Isotropic curvature adds a constant value on the sphere and contributes no variation, regardless of magnitude. Neither τ_a nor a bound on it is a decoder input or a restriction on candidate offsets.

Theorem 2 (Whole-cell localization with unknown even nuisance)**.** *There are absolute constants $c, C > 0$ such that the following holds. Let $d \geq 3$, $0 < \varepsilon \leq 1/10$, $0 < \delta \leq 1/4$, and fix any even instance with $\tau \leq c\varepsilon/\sqrt{d}$. Set*

$$L_\varepsilon = d\log(C\sqrt{d}/\varepsilon) + \log(C/\delta), \qquad n \geq C\big(L_\varepsilon + \sqrt{L_\varepsilon/\varepsilon}\big). \tag{8}$$

The complete ranking of $2n$ paid endpoints $\pm aW_i$, with independent uniform $W_i \in \mathbb{S}^{d-1}$, satisfies $\mathbb{P}\{u \in \mathcal{C} \subseteq \mathcal{C}_{\mathrm{rev}} \subseteq \mathcal{B}(u, \varepsilon)\} \geq 1 - \delta$.

Every consistent estimate is accurate on this event, and the direction set has diameter at most 2ε. Reverse alone achieves the rate. In contrast, one-round sign-only recovery has minimax cost $\Theta(d/\varepsilon)$ even on the zero-variation isotropic subclass (Corollary 7 and Appendix D.2). Here n counts pairs and $N = 2n$ counts endpoints.

Why dependent comparisons still help. A direction v at angle at least ε from u is ruled out by a pair with opposite projection margins:

$$u^\top(W_j - W_i) \geq c_1\varepsilon/\sqrt{d}, \qquad v^\top(W_j - W_i) \leq -c_2\varepsilon/\sqrt{d}. \tag{9}$$

The true gap exceeds nuisance variation, forcing reverse orders that exclude v. Endpoint-disjoint witnesses from adjacent projection spacings and separated central quantile blocks yield failure terms of order $e^{-cn^2\varepsilon}$ and e^{-cn}. A finite net excludes all distant directions when $n^2\varepsilon \gtrsim L_\varepsilon$ and $n \gtrsim L_\varepsilon$, without assuming independence of all comparisons (Appendix B).

Near-optimality and degradation with scale. The known isotropic family $q_u(x) = u^\top x + \|x\|^2/2$ already requires $\Omega(d + \sqrt{d/\varepsilon})$ one-round endpoints, allowing arbitrary radii. Counting regions cut by $O(N^2)$ pairwise equality hyperplanes gives the square-root term. The dimension term holds even with numerical values, which reveal only linear measurements after subtracting the known quadratic (Appendix C).

At the sample count for nominal accuracy ε, the sufficient enclosing radius becomes $\varepsilon_{\mathrm{out}} = \max\{\varepsilon, C\sqrt{d}\,\tau_a\}$ whenever $\varepsilon_{\mathrm{out}} \leq 1/10$, with probability at least $1 - \delta$ (Appendix B.3.3). This is not an accuracy floor: exact Mirror signs still permit finer recovery with more endpoints.

3.2 Unbounded relative curvature can erase the gain

A small condition number does not replace a relative-scale bound. For any prescribed $\kappa > 1$, consider

$$\mathcal{Q}_{d,\kappa} = \{b + u^\top x + \tfrac{1}{2}x^\top Hx : \|u\| = 1,\ H \succ 0,\ \mathrm{cond}(H) < \kappa\}, \tag{10}$$

with no common bound on $\|H\|$. Let $N_\star(d, \varepsilon, R)$ be the least hard endpoint budget satisfying Equation (2) on this class.

Table 1: Complexity bounds at fixed confidence. The favorable condition concerns actual shell variation, not candidate offsets. The Mirror bound uses the same class. Only the pairwise benchmark counts comparisons; other rows count endpoints. Unbounded scale defines a different class.

Instance / information used	Rounds	Reported bound
Even nuisance, $\tau \le c\varepsilon/\sqrt{d}$; Reverse	1	$O(L_\varepsilon + \sqrt{L_\varepsilon/\varepsilon})$
Known isotropic quadratic; complete ranking	1	$\Omega(d + \sqrt{d/\varepsilon})$
Even nuisance, $\tau \le c\varepsilon/\sqrt{d}$; Mirror	1	$\Theta(d/\varepsilon)$
Supplied-smoothness pairwise recovery (Tao et al., 2026)	adaptive	$\Theta(d\log(1/\varepsilon))$
Unbounded quadratic scale; complete ranking	R	$\Theta(dR(\varepsilon^{-1/R}-1))$

Theorem 3 (Cumulative-ranking scale barrier)**.** *For $d \ge 3$, $0 < \varepsilon \le 1/10$, and integer $R \ge 1$, under either ranking oracle,*

$$N_\star(d,\varepsilon,R) = \Theta\big(dR(\varepsilon^{-1/R}-1)\big), \tag{11}$$

with absolute constants uniform over every prescribed $\kappa > 1$. The lower bound allows arbitrary radii, adaptive batch sizes, early stopping, and randomized queries.

The lower bound uses $H = tA$ with A arbitrarily close to I. With high probability, one sufficiently large deterministic t makes curvature dominate every non-antipodal, non-repeated comparison throughout the algorithm's finite query tree. Only antipodal signs then depend on the gradient, even cumulatively. The instance distribution is independent of the realized private seed. Each new endpoint reveals at most one new sign, including pairs completed against old endpoints. Sign-arrangement counting and a finite Mirror construction give matching bounds (Appendix D).

One round costs $\Theta(d/\varepsilon)$. Sufficiently many rounds reduce this to $\Theta(d\log(1/\varepsilon))$ (Table 1). Although $\tau_a \to 0$ as $a \to 0$ for each fixed differentiable even instance, this convergence is not uniform over the class (Appendix A.1). Shrinking radii can help a fixed instance without defeating the uniform hard-budget barrier.

3.3 Calibrated recovery beyond exact evenness

Evenness is essential for zero-error validity. On a radius-a sphere, the odd cubic $\mu(q^\top x)\,\|x\|^2$ equals the linear term $\mu a^2 q^\top x$, despite having zero gradient at the center. A small fitted set can therefore exclude the true direction. Adding smaller-shell constraints cannot restore an excluded direction (Proposition 10).

For normalized scores $e_i \pm (u^\top W_i + o_i)$ with a supplied bound $|o_i| \le \rho$, fit free even offsets and one shared candidate error $b_i \in [-\rho,\rho]$ per pair. The true direction remains feasible, and the endpoint count of Theorem 2 localizes the whole set when $\tau_a + \rho \le c\varepsilon/\sqrt{d}$ (Corollary 8). This is a shared-score model, not one of independent edge errors or arbitrary cyclic judgments.

For noiseless rankings, an L-Lipschitz gradient on a radius-a_0 ball and a supplied bound $\|g\| \ge g_{\min} > 0$ permit

$$0 < a \le \min\{a_0, c_0\varepsilon g_{\min}/(L\sqrt{d})\}, \qquad \rho = La/(2g_{\min}). \tag{12}$$

This gives whole-cell recovery without exact evenness or a third-derivative bound (Corollary 9). Appendix J.3 gives an empirical check. Alternatively, supplied third-derivative and endpoint score-error bounds M_3 and ν give $\rho = M_3 a^2/(6g_{\min}) + \nu/(ag_{\min})$. Smaller probes reduce the odd remainder but amplify normalized score error, which also enlarges the even-offset range (Appendix E). These calibration inputs are not inferred from ranks; a small fitted set cannot validate them.

4 Experiments: From Information to Task Progress

Design and evaluation. We separately evaluate direction-set information, squared angular error, and optimization progress. Synthetic objectives control nuisance scale and rank. Ridge tasks test optimization, and non-even logistic tasks test calibrated validity (Section 4.4). Exact-even recovery uses only coordinates and ranks. Gradients, optima, and held-out losses are audit quantities. Real-data studies impose ranking interfaces on ordinary objectives rather than on intrinsically ordinal datasets.

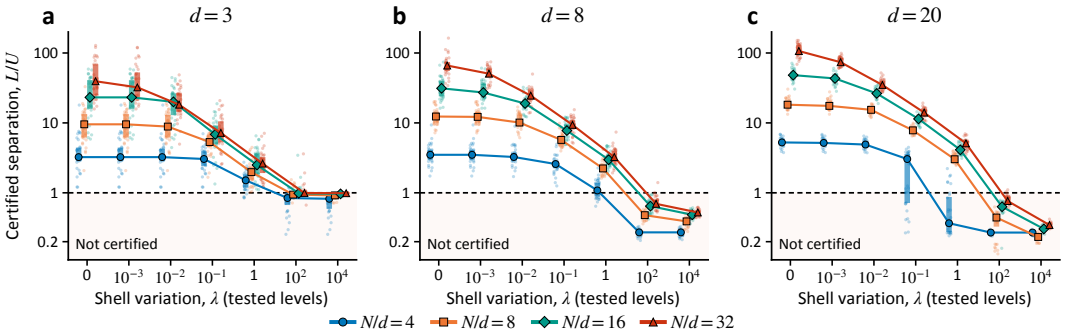

Figure 2: Ranking information on matched endpoints. $L/U > 1$ certifies separation; its absence does not establish equality. Radius-U caps enclose Reverse and Full. Medians and interquartile bands use 32 shared targets per dimension. Shell-variation levels are tested categories. Lines guide the eye.

Each real-data task fixes an 80/20 split with training-only standardization. Tuning uses separate development seeds. Direction error is measured by mean squared angular error (MSE). Ratios compare arithmetic means. Resampling preserves repeated settings within each independent target or algorithm seed. Intervals do not quantify dataset or split variation. Synthetic comparisons share designs; moving-center comparisons share observations only while centers coincide. External controls use native queries. Comparisons evaluate complete procedures. Protocols are in Appendices G to K.

4.1 When do rankings reveal more than signs?

Let U be a checked outer-cap radius for Reverse and hence Full. Two Mirror-feasible directions separated by $2L$ give a lower bound L on any cap enclosing Mirror. Hence $U < L$ certifies additional information independently of the selected direction. The exact Full projection is audited separately in three dimensions (Appendix G.1.4).

Uniform antipodal batches use $N/d \in \{4, 8, 16, 32\}$ and $H = 100\lambda(I + 0.02zz^\top)$, $\|z\| = 1$. Positive scales have condition number 1.02 and nominal unit-shell variation λ; at zero, $H = I$. The design reuses 96 independent target–axis units, 32 at each $d = 3, 8, 20$. Separation holds in all 384 conditions at each of $\lambda = 0, 10^{-3}, 10^{-2}$, then in 375, 341, 31, and zero at $10^{-1}, 1, 10^2, 10^4$ (Figure 2).

True-direction feasibility and cap coverage hold throughout. At $\lambda = 10^4$, all 64 exact checks at $d = 3$, $N/d = 8, 32$ establish Full–Mirror equality. Thus information gain can disappear without invalidating the model. All 576 quartic even conditions also retain the true direction and certify separation (Appendix G.2). An independent first-batch audit appears in Appendix G.4. These tests illustrate the mechanism, not fitted asymptotic rates or a calibrated theorem threshold.

4.2 Beyond short cycles under higher-rank anisotropy

Recovery under rank-one anisotropy can become easier as the dimension grows. To test a harder nuisance geometry, we compare

$$f_k(x) = g^\top x + 50\lambda \|x\|^2 + \lambda \left\|P_k Q^\top x\right\|^2, \qquad k \in \{1, d/2\}, \tag{13}$$

where Q is a rational orthogonal reflection and P_k selects k coordinates, giving anisotropic rank k. Both families have Hessian eigenvalues ranging from 100λ to 102λ and nominal unit-shell variation λ. At fixed $\lambda/\|g\|$, the nuisance-to-signal standard-deviation ratio under uniform spherical queries decays as $d^{-1/2}$ for rank one but stays of constant order for rank $d/2$ (Appendix G.3).

Twelve independent target–reflection–design units, four at each $d = 8, 20, 50$, are reused across $N/d = 8, 16$, $\lambda = 10^{-3}, 10^{-1}, 1$, and both ranks. All 432 model outputs are feasible, and all 144 conditions certify separation between Full and Mirror. Exact negative cycles establish strict inclusion of Full in Reverse in 49/72 rank-one and 55/72 high-rank conditions (Figure 3). A separate frozen-rule cohort confirms both types of information gain (Appendix G.3).

MSE also depends on the analytic-center selector; the exact cycle witnesses do not. With four independent units per dimension, rank-dependent MSE contrasts are exploratory (Appendix G.3.2).

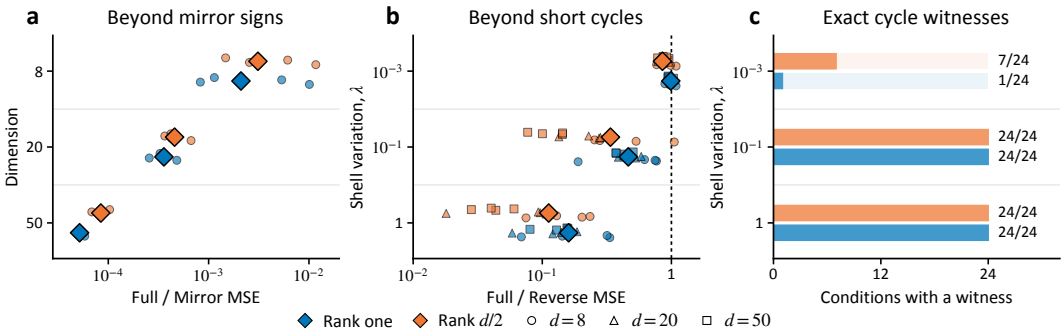

Figure 3: Matched anisotropic ranks. (a, b) Diamonds and small points show pooled and within-unit MSE ratios, respectively. (c) Negative cycles certify strict inclusion of Full in Reverse; absence is inconclusive. Only the primary cohort is shown (Appendix G.3.2).

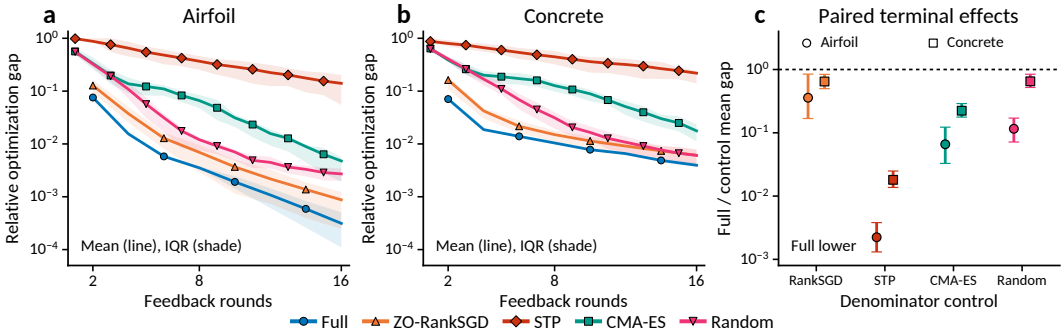

Figure 4: Optimization under endpoint and sixteen-round caps. (a, b) Curves show the arithmetic mean relative gaps over 32 seeds. (c) Full/control terminal mean-gap ratios have Bonferroni-adjusted 95% intervals over sixteen cross-profile contrasts. Equal caps need not imply equal realized endpoints.

4.3 Which information layer helps optimization?

The UCI Airfoil Self-Noise and Concrete Compressive Strength ridge tasks have $d = 6, 9$, including the intercept (Brooks et al., 1989; Yeh, 1998). Both use a feature penalty of 0.01 and no Hessian whitening. Squared loss is exactly linear-plus-even at every center. The recovery model is rebuilt after each move. Progress is the remaining relative training gap $r(\theta) = [F(\theta) - F^\star]/[F(\theta_0) - F^\star]$, where $F^\star$ is reserved for evaluation.

Matched inference layers. Mirror, Reverse, and Full share query draws and the unit-direction step grid $\{0, 2^{-10}, \ldots, 2^1\}$. Each update pays $8d$ recovery endpoints and thirteen step candidates in two rounds. Eight updates use $488/680$ endpoints and sixteen rounds on Airfoil/Concrete. Two prespecified shared radii, $1/8$ and $1/64$, and 32 paired seeds per task give 384 trajectories. Full improves over Mirror at both Concrete radii, while the Airfoil comparisons are inconclusive. No Full/Reverse interval excludes one (Table 2, panel A).

We compare Full with ranking-based zeroth-order stochastic gradient descent (ZO-RankSGD) (Tang et al., 2024), stochastic three points (STP) (Bergou et al., 2020), the covariance matrix adaptation evolution strategy (CMA-ES) (Hansen & Ostermeier, 2001), and local incumbent random search (Random). Each uses native queries and returns the best paid point via an ordinal incumbent update. Separate development seeds tune each procedure, including round-aware CMA-ES populations. Evaluation uses 32 seeds per split (Appendix H.3).

An additional incumbent evaluation raises the endpoint caps to $489/681$, still with sixteen rounds. Full and ZO-RankSGD reach these caps, while sequential STP uses only 33 endpoints. Thus STP is constrained by rounds, not matched in realized evaluations. ZO-RankSGD and round-aware CMA-ES are the batch-capable controls. All eight displayed adjusted Full/control intervals lie below one (Figure 4). Adjustment covers sixteen contrasts across both resource profiles (Appendix H.5).

Table 2: Terminal mean-gap ratios. Paired 95% intervals use 32 seeds per split and Bonferroni adjustment (Appendices H.2 and H.5). Values below one favor the numerator; intervals containing one do not establish equivalence.

Comparison	Airfoil	Concrete
A. Matched inference layers; sixteen-round trajectories		
Full / Mirror, $a = 1/8$	$0.562\ [0.221, 1.482]$	$0.742\ [0.625, 0.884]$
Full / Mirror, $a = 1/64$	$0.437\ [0.175, 1.237]$	$0.734\ [0.621, 0.864]$
Full / Reverse, $a = 1/8$	$0.892\ [0.592, 1.331]$	$1.027\ [0.952, 1.109]$
Full / Reverse, $a = 1/64$	$0.993\ [0.720, 1.371]$	$1.000\ [0.923, 1.084]$
B. Independently tuned methods; joint endpoint–round caps		
Full / Reverse	$0.956\ [0.767, 1.185]$	$1.003\ [0.929, 1.081]$
Reverse / ZO-RankSGD	$0.374\ [0.179, 0.823]$	$0.645\ [0.512, 0.823]$
Reverse / CMA-ES	$0.0689\ [0.0354, 0.1250]$	$0.223\ [0.172, 0.292]$

Table 3: Optimization without a round cap. Gaps are arithmetic means over 32 seeds; parentheses give feedback rounds. Endpoint counts are Airfoil/Concrete. Table 5 gives the full resource ledger.

Method	Endpoints (A/C)	Airfoil: gap (rounds)	Concrete: gap (rounds)
Full	489/681	3.13×10^{-4} (16)	3.95×10^{-3} (16)
ZO-RankSGD	489/681	8.75×10^{-4} (16)	6.11×10^{-3} (16)
STP	489/681	$\mathbf{1.43 \times 10^{-5}}$ (244)	6.60×10^{-4} (340)
CMA-ES	487/681	1.58×10^{-5} (54)	$\mathbf{1.85 \times 10^{-4}}$ (68)
Random	489/681	2.57×10^{-3} (17)	8.02×10^{-3} (17)

Do longer cycles explain these gains? Independently tuning Reverse with Full's grid, development budget, query generator, line search, and return rule selects the same configurations: radius $1/64$ on Airfoil and $1/16$ on Concrete. These differ from the shared-radius design above. All 128 paired first batches match exactly. Reverse retains the adjusted gains over both batch-capable controls, while Full/Reverse intervals for terminal gap and test root mean squared error (RMSE) include one (Table 2, panel B; Appendix H.5). The tested ridge protocols therefore do not establish an additional optimization benefit from longer-cycle fitting.

These are pipeline comparisons, not isolated estimator comparisons. ZO-RankSGD is not unit-normalized before line search, and the ridge study lacks a normalized control or a Mirror external-control arm. Incomplete tuning details further limit attribution (Appendix H.3).

Removing the round cap. Under endpoint-only caps, STP and CMA-ES attain lower mean gaps than Full on both tasks, using 54–340 rounds rather than sixteen (Table 3 and Appendix H.4). This descriptive reversal locates the observed advantage in feedback-scarce settings. On these inexpensive objectives, both recovery procedures take longer to run than ZO-RankSGD, and training-gap reductions do not yield comparable improvements in test RMSE (Appendix H.5).

4.4 Does calibrated recovery retain the true gradient?

The UCI Blood Transfusion Service Center (Blood) and Banknote Authentication (Banknote) tasks ($d = 4, 5$) use nonzero intercepts to avoid the exactly linear-plus-even expansion at zero (Yeh, 2008; Lohweg, 2012). Thirty-two dataset–seed units across four radii and two noise levels give 256 conditions. Zero-error Full, robust Reverse, and robust Full share $8d$ antipodal endpoints, including paid initialization, in one recovery round. Supplied error envelopes preserve true-direction feasibility and cap coverage in every robust fit. Zero-error Full excludes the true direction thirteen times, including three without score noise.

At $\nu = 10^{-5}$, mean outer caps for robust Full shrink as a decreases from $1/4$ to $1/32$, then increase at $1/128$, consistent with the competing remainder and score-error allowances (Figure 5 and Appendix I.3). The paid initializer accepts only a checked factor-two error inflation. Its success is not established throughout the full robust-localization regime (Appendices F.5 and J.4). Metadata-based calibration, local-step controls, and synthetic validity tests are in Appendices I and J.

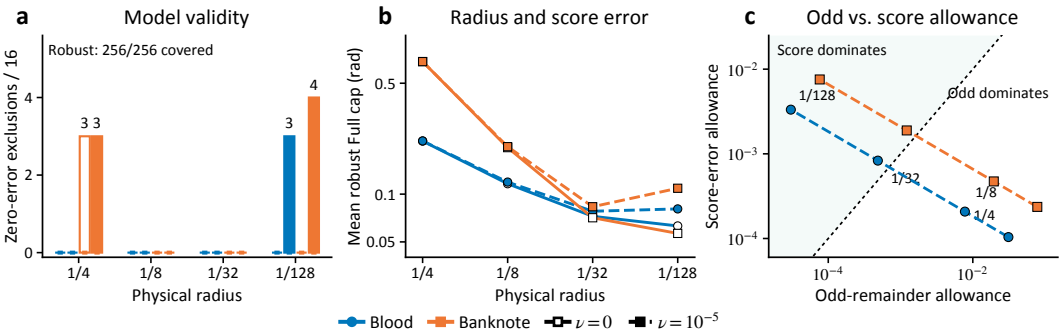

Figure 5: Calibrated non-even recovery. (a) Counts show true-direction exclusions by zero-error Full (sixteen seeds per task–radius–noise cell). (b) Curves show mean outer-cap radii for robust Full. (c) Axes show score-error and odd-remainder allowances at $\nu = 10^{-5}$ (Appendix I.3).

5 Related Work

Comparison-based recovery. Frame-coefficient orderings support unit-vector reconstruction (Nguyen et al., 2011), and binary function comparisons estimate gradient directions (Cai et al., 2022). With supplied smoothness and a gradient-norm lower bound, adaptive pairwise recovery attains optimal $\Theta(d \log(1/\varepsilon))$ comparison complexity (Tao et al., 2026). Radius adaptation without a supplied regularity scale (Scheinberg & Xiong, 2026) and normalized-Hessian estimation for stationarity (Wang et al., 2026) address questions distinct from characterizing the full consistent set of a single ranked batch.

Ordinal optimization. Rankings and batch winners guide optimization (Tang et al., 2024; Saha et al., 2024; 2025). Preferences also support surrogate search (Xu et al., 2024; Zhang et al., 2025), policy gradients, and ordinal reward modeling (Zhang & Ying, 2025; Afsharrad et al., 2026). Our goal is to characterize all constraints implied by shared pair offsets. The calibrated model preserves transitive shared scores, unlike the observation models of variance-aware and corruption-robust dueling (Di et al., 2024; Cheng et al., 2025).

Numerical-value methods. Two-point estimators (Duchi et al., 2015), sparse or directionally aligned estimates (Chen et al., 2024; Ma & Huang, 2025), Hessian-informed updates (Zhao et al., 2025; Li et al., 2026), and low-rank fine-tuning (Chen et al., 2025) use numerical values unavailable to our decoder. Generalization and privacy require separate analyses (Liu et al., 2024; Zhang et al., 2024).

6 Discussion and Conclusion

The shell-variation condition is sufficient, not necessary, and cannot be verified from rankings alone. Joint dimension–round optimality in the favorable regime, observable radius selection, and optimization convergence are not established here. Fixed-center guarantees do not justify transferring constraints to a new gradient. Non-even recovery requires supplied calibration, and outer caps can be conservative. The task evidence covers four low-dimensional datasets with fixed splits.

Computation can outweigh endpoint savings. At $d = 100$ and $N = 1600$, median fitting and certification take 1.64 and 142.55 seconds, respectively (Table 12). Certification is optional, and no end-to-end break-even point is established. Information gain, point-estimation error, and practical optimization cost therefore need separate evaluation.

Rankings beat signs by cancelling shared offsets. Small relative shell variation makes Reverse's short-cycle constraints sufficient for nearly optimal one-round whole-cell recovery, even without a shell-variation bound supplied to the decoder. Unbounded relative curvature can erase this gain on well-conditioned positive-definite quadratics, even with cumulative rankings. Matched-endpoint experiments certify additional information in Full beyond Mirror and Reverse, including under higher-rank anisotropy. On the two ridge tasks under joint endpoint–round caps, Reverse attains lower terminal mean gaps than the tested batch-capable ZO-RankSGD and round-aware CMA-ES pipelines. The ridge experiments do not establish an additional optimization benefit from longer-cycle fitting.

AI USE STATEMENT

We used AI assistants to implement and debug experimental code, prepare figures, and provide feedback on the evaluation framework and experimental protocols. Writing assistance primarily involved language polishing and condensation of author-written text, with limited drafting and rewriting of selected passages based on author-provided content. AI assistants also supported selected mathematical derivations and proof development. The authors reviewed the AI-assisted text and code and verified reported results against experimental outputs. The authors made the final methodological decisions and take full responsibility for the scientific claims and the accuracy and integrity of the manuscript and accompanying artifacts.

ETHICS STATEMENT

This work develops and evaluates a methodology for comparison-based optimization. The empirical studies use synthetic objectives and existing public benchmark datasets. No new human-subject data were collected as part of this work. The experiments are methodological evaluations and do not involve deployment in clinical or other high-stakes decision-making settings.

REPRODUCIBILITY STATEMENT

Appendices A to E provide the assumptions and proofs. Appendix F specifies the numerical certificate. The experimental protocols and resource accounting appear in Appendices G to K. The anonymous supplementary material includes companion data, per-run records, seed/split manifests, and executable experiment and checker code. These materials support independent reproduction of the reported numerical audits, summaries, and figures.

REFERENCES

Amirhossein Afsharrad, Ruida Zhou, Luca Viano, Sanjay Lall, and Mohammad Ghavamzadeh. Beyond binary preferences: A principled framework for reward modeling with ordinal feedback. In *International Conference on Learning Representations*, pp. 119472–119505, 2026.

El Houcine Bergou, Eduard Gorbunov, and Peter Richtárik. Stochastic three points method for unconstrained smooth minimization. *SIAM Journal on Optimization*, 30(4):2726–2749, 2020. doi: 10.1137/19M1244378.

Thomas Brooks, D. Pope, and Michael Marcolini. Airfoil self-noise. UCI Machine Learning Repository, 1989. Dataset.

HanQin Cai, Daniel McKenzie, Wotao Yin, and Zhenliang Zhang. A one-bit, comparison-based gradient estimator. *Applied and Computational Harmonic Analysis*, 60:242–266, 2022. doi: 10.1016/j.acha.2022.03.003.

Aochuan Chen, Yimeng Zhang, Jinghan Jia, James Diffenderfer, Konstantinos Parasyris, Jiancheng Liu, Yihua Zhang, Zheng Zhang, Bhavya Kailkhura, and Sijia Liu. DeepZero: Scaling up zeroth-order optimization for deep model training. In *International Conference on Learning Representations*, pp. 50185–50206, 2024.

Yiming Chen, Yuan Zhang, Liyuan Cao, Kun Yuan, and Zaiwen Wen. Enhancing zeroth-order fine-tuning for language models with low-rank structures. In *International Conference on Learning Representations*, pp. 62581–62607, 2025.

Yuwei Cheng, Fan Yao, Xuefeng Liu, and Haifeng Xu. Learning from imperfect human feedback: A tale from corruption-robust dueling. In *International Conference on Learning Representations*, pp. 29795–29826, 2025.

Thomas H. Cormen, Charles E. Leiserson, Ronald L. Rivest, and Clifford Stein. *Introduction to algorithms*. Cambridge, MA, USA, 2001.

Qiwei Di, Tao Jin, Yue Wu, Heyang Zhao, Farzad Farnoud, and Quanquan Gu. Variance-aware regret bounds for stochastic contextual dueling bandits. In *International Conference on Learning Representations*, 2024.

John C. Duchi, Michael I. Jordan, Martin J. Wainwright, and Andre Wibisono. Optimal rates for zero-order convex optimization: The power of two function evaluations. *IEEE Transactions on Information Theory*, 61(5):2788–2806, 2015. doi: 10.1109/TIT.2015.2409256.

Jean-Louis Goffin and Jean-Philippe Vial. Convex nondifferentiable optimization: A survey focused on the analytic center cutting plane method. *Optimization Methods and Software*, 17(5):805–867, 2002. doi: 10.1080/1055678021000060829a.

Nikolaus Hansen and Andreas Ostermeier. Completely derandomized self-adaptation in evolution strategies. *Evolutionary Computation*, 9(2):159–195, 2001. doi: 10.1162/106365601750190398.

Wassily Hoeffding. Probability inequalities for sums of bounded random variables. *Journal of the American Statistical Association*, 58(301):13–30, 1963. doi: 10.1080/01621459.1963.10500830.

Zhe Li, Bicheng Ying, Zidong Liu, Chaosheng Dong, and Haibo Yang. Converge faster, talk less: Hessian-informed federated zeroth-order optimization. In *International Conference on Learning Representations*, 2026.

Xinyue Liu, Hualin Zhang, Bin Gu, and Hong Chen. General stability analysis for zeroth-order optimization algorithms. In *International Conference on Learning Representations*, 2024.

Aleksandr Lobanov, Alexander Gasnikov, and Andrei Krasnov. Acceleration exists! Optimization problems when oracle can only compare objective function values. In *Advances in Neural Information Processing Systems*, pp. 21428–21460, 2024.

Volker Lohweg. Banknote authentication. UCI Machine Learning Repository, 2012. Dataset.

Shaocong Ma and Heng Huang. Revisiting zeroth-order optimization: Minimum-variance two-point estimators and directionally aligned perturbations. In *International Conference on Learning Representations*, pp. 13267–13293, 2025.

Tom M. Mitchell. Generalization as search. *Artificial Intelligence*, 18(2):203–226, 1982. doi: 10.1016/0004-3702(82)90040-6.

Ha Q. Nguyen, Vivek K. Goyal, and Lav R. Varshney. Frame permutation quantization. *Applied and Computational Harmonic Analysis*, 31(1):74–97, 2011. doi: 10.1016/j.acha.2010.10.003.

R. Pyke. Spacings. *Journal of the Royal Statistical Society: Series B (Methodological)*, 27(3): 395–436, 1965. doi: 10.1111/j.2517-6161.1965.tb00602.x.

Yuxuan Ren, Abhishek Roy, and Shiqian Ma. Riemannian dueling optimization. In *Proceedings of the 43rd International Conference on Machine Learning*, 2026.

Aadirupa Saha, Vitaly Feldman, Yishay Mansour, and Tomer Koren. Faster convergence with multiway preferences. In *Proceedings of the 27th International Conference on Artificial Intelligence and Statistics*, pp. 433–441, 2024.

Aadirupa Saha, Tomer Koren, and Yishay Mansour. Dueling convex optimization with general preferences. In *Proceedings of the 42nd International Conference on Machine Learning*, pp. 52552–52564, 2025.

Katya Scheinberg and Zikai Xiong. Function-free optimization via comparison oracles, 2026.

Zhiwei Tang, Dmitry Rybin, and Tsung-Hui Chang. Zeroth-order optimization meets human feedback: Provable learning via ranking oracles. In *International Conference on Learning Representations*, pp. 13941–13971, 2024.

Xiwen Tao, Chenyi Zhang, Helin Wang, Yexin Zhang, and Tongyang Li. Gradient testing and estimation by comparisons. In *Proceedings of the 43rd International Conference on Machine Learning*, 2026.

Helin Wang, Chenyi Zhang, Xiwen Tao, Yexin Zhang, and Tongyang Li. Finding stationary points by comparisons. In *Proceedings of the 43rd International Conference on Machine Learning*, 2026.

Wenjie Xu, Wenbin Wang, Yuning Jiang, Bratislav Svetozarevic, and Colin Jones. Principled preferential Bayesian optimization. In *Proceedings of the 41st International Conference on Machine Learning*, pp. 55305–55336, 2024.

I-Cheng Yeh. Concrete compressive strength. UCI Machine Learning Repository, 1998. Dataset.

I-Cheng Yeh. Blood transfusion service center. UCI Machine Learning Repository, 2008. Dataset.

Qining Zhang and Lei Ying. Zeroth-order policy gradient for reinforcement learning from human feedback without reward inference. In *International Conference on Learning Representations*, 2025.

Qinzi Zhang, Hoang Tran, and Ashok Cutkosky. Private zeroth-order nonsmooth nonconvex optimization. In *International Conference on Learning Representations*, 2024.

Xinyu Zhang, Daolang Huang, Samuel Kaski, and Julien Martinelli. PABBO: Preferential amortized black-box optimization. In *International Conference on Learning Representations*, 2025.

Yanjun Zhao, Sizhe Dang, Haishan Ye, Guang Dai, Yi Qian, and Ivor W. Tsang. Second-order fine-tuning without pain for LLMs: A Hessian informed zeroth-order optimizer. In *International Conference on Learning Representations*, 2025.

Appendix

CONTENTS

A Model Validity and the Geometry of Ranking Constraints **15**
A.1 Normalization, closure, and nuisance gauges 15
A.2 Cycle characterization and short-cycle certificates 15
A.3 A measurable consistent selector 16

B Proof of Whole-Cell Localization **16**
B.1 Projection regularity for uniform queries 16
B.2 Separated witnesses from dependent rankings 17
B.3 Whole-cell localization 18

C Lower Bounds in the Small-Variation Regime **19**

D The Unbounded-Scale Endpoint–Round Barrier **21**
D.1 The cumulative-ranking lower bound 21
D.2 A finite Mirror construction for matching achievability 22

E Model Error, Ambiguity, and Valid Retention **24**
E.1 Calibrated localization: formal statements 24
E.2 Why an exact-even fit can fail outside its model 24
E.3 A full shared-error model and its localization result 24
E.4 From score noise and local smoothness to an error envelope 26

F Fitting and Certifying the Direction Set **26**
F.1 A bounded section in gradient variables 26
F.2 Transitive reduction and certificate completion 27
F.3 Joint analytic centers and their sections 28
F.4 Feasible enclosing centers in three dimensions 29
F.5 A computable chart that contains the robust Full model 29

G Information Geometry: Scale, Nuisance Rank, and Cycles **31**
G.1 Structural experiments: protocol 31
G.2 Structural experiments: supporting results 32
G.3 Matched rank-one and higher-rank anisotropy 33
G.4 Additional independent first-batch information audit 35

H Ranking-Only Optimization on Real-Data Quadratic Tasks **35**
H.1 Tasks, information access, and the local model 35

H.2 Information-layer trajectories 36
H.3 External optimizer implementations and development 36
H.4 Endpoint and feedback-round accounting 37
H.5 Effects and statistical scope 37

I Non-Even Logistic Recovery and Local-Step Controls **38**
I.1 Tasks and nonzero recovery centers 38
I.2 Public smoothness, third derivative, and gradient calibration 39
I.3 Matched recovery-stage validity 39
I.4 Matched-budget local-step comparisons and physical-step control 40
I.5 Direction accuracy and downstream loss are separate outcomes 40

J Validity Tests under Odd Remainders and Score Noise **41**
J.1 Odd remainders: containment, coverage, and history 41
J.2 Matched error-contract experiments 42
J.3 A non-even smooth objective with a public radius 43
J.4 Observable initialization and retained recovery 44
J.5 Task-structured gradient calibration for noisy squared loss 45

K Computational Cost and Higher-Dimensional Recovery **45**
K.1 Stored constraints and numerical work 45
K.2 A controlled dimension–budget study 46

APPENDIX GUIDE

Appendix A develops the information model, and Appendices B to D establish the two information regimes. Calibration and numerical certificates are in Appendices E and F. The experiments cover matched-endpoint information geometry (Appendix G), regression optimization and resource attribution (Appendix H), non-even logistic validity and local-step controls (Appendix I), and synthetic validity and initialization (Appendix J). Appendix K reports computational costs. Primary and confirmation cohorts are kept separate.

Audit trail and artifact availability. The CSV/JSON paths below locate the supporting records in the anonymous supplementary material. Reproduction has three stages. First, regenerate the paid coordinates and rankings from the frozen task, split, and seed specifications. Second, check feasibility, cycle witnesses, error contracts, and support bounds independently of the fitting solver. Third, recompute the stated summaries with the original grouping and resampling units. A cycle check needs the candidate direction, ordered edges, and exact weights. A cap check needs the section, support directions, dual multipliers, and residual allowances. The rational example in Appendix A.2 is fully specified in the text.

A Model Validity and the Geometry of Ranking Constraints

A.1 Normalization, closure, and nuisance gauges

For a differentiable even E, $\nabla E(0) = 0$. The directional derivatives in opposite directions are equal by evenness and opposite by differentiability, hence zero. Therefore g in the model is the actual gradient at the fixed center. Dividing all scores by $\|g\| > 0$ and subtracting $b/\|g\|$ gives Equation (3). On one physical shell $x_i = aW_i$, further division by a gives normalized scores $\sigma u^\top W_i + E(aW_i)/(a\|g\|)$. Across shells, the common normalization by $\|g\|$ retains all physical coordinates and every cumulative ranking relation. Every true ranking relation is satisfied by (u, e). Exact antipodality, rather than equality of nuisance values across different pairs, is the required structure.

The candidate vector v may be any nonzero vector before normalization. The cone K is positively homogeneous in (v, z), so its unit-direction projection is exactly Equation (5). The projection $G = \mathrm{proj}_v K$ of the finite polyhedral cone is polyhedral and closed, so $\mathcal{C} = G \cap \mathbb{S}^{d-1}$ is compact. No boundedness of the joint cone is assumed. Adding a common constant to every z_i leaves all inequalities unchanged. A common gauge, such as $z_1 = 0$, removes this lineality. If only batch orders are retained, their disconnected components can have separate additive gauges. Cumulative orders connect the observed endpoints and use a common gauge. Repeated physical pairs always share their nuisance coordinate.

Replacing a strict observed order by a weak candidate inequality enlarges the strict consistency set. All upper bounds control this closed relaxation, including boundary directions with candidate ties. Tied observations impose both weak inequalities. No numerical equality is inferred from finite precision. Repeated pairs and mathematical ties do not affect the validity argument.

Instancewise small-radius limit. Differentiability and evenness give $\nabla E(0) = 0$ and $E(x) = E(0) + o(\|x\|)$. Thus

$$\Omega_a(E) \le 2 \sup_{\|x\|=a} |E(x) - E(0)| = o(a), \qquad \tau_a \longrightarrow 0.$$

The quadratic subclass permits arbitrarily large anisotropic curvature, so convergence to this favorable regime is not uniform over the full class.

A.2 Cycle characterization and short-cycle certificates

The relation $(i, \sigma) \preceq (j, \zeta)$ is equivalent to

$$z_i \le z_j + w_{ji}(v), \qquad w_{ji}(v) = \zeta v^\top x_j - \sigma v^\top x_i. \tag{14}$$

Create an edge $j \to i$ of this weight. Summing around a directed cycle cancels the potentials, so a feasible z requires every cycle to have nonnegative weight. Conversely, add an auxiliary source with zero-weight edges to all vertices. If there is no negative cycle, shortest-path distances from that source are finite and satisfy Equation (14). They supply a feasible potential. This is the standard difference-constraint characterization (Cormen et al., 2001), including self-loops and disconnected components. For a system of strict inequalities, all directed simple cycles must have positive weight. Subtracting a common positive number smaller than their minimum mean weight reduces sufficiency to the weak case. An acyclic graph permits any positive subtraction.

When positive endpoints are ordered increasingly and their negatives decreasingly, the two inequalities are

$$v^\top(x_j - x_i) + (z_j - z_i) \ge 0, \qquad v^\top(x_j - x_i) - (z_j - z_i) \ge 0.$$

Their sum gives the Reverse constraint in Equation (4). Orienting either unsigned pair differently also gives rows proportional to $x_i + x_j$. The certifying outer cone retains all valid signed orientations and the self-loop Mirror rows. The localization proofs need only the positive-positive reverse relations. If E is constant on the shell, every strict order of positive linear projections has the reverse order on the negative endpoints. The same unrestricted model consequently inherits all those linear-ranking inequalities, without requiring equal candidate potentials.

A concrete longer-cycle example. For unsigned points e_1, e_2, e_3, take $g = (1/5, 4/5, 1/5)$, $H = \mathrm{diag}(7/5, 2, 13/5)$, and $f(x) = g^\top x + x^\top Hx/2 - 1$. Then

$$f(-e_2) = -4/5 < f(-e_1) = -1/2 < f(e_1) = -1/10 \\ < f(-e_3) = 1/10 < f(e_3) = 1/2 < f(e_2) = 4/5.$$

Mirror rows require positive coordinates, and the two-edge relations require the second coordinate to exceed each of the first and third. The two separated inner intervals impose no comparison between their widths. The candidate $(1/2, 4/5, 1/2)$ satisfies these short-cycle restrictions. Yet the outer mirror interval for pair 2 contains the two disjoint intervals for pairs 1 and 3. Its width must be at least their sum in the closed model, requiring $v_2 \geq v_1 + v_3$, which this candidate violates. Hence Full can be strictly smaller than its Reverse outer approximation. Normalization preserves these homogeneous restrictions. For this candidate, the adjacent-order edges $1 \to 2$, $2 \to 3$, and $3 \to 1$ in Equation (14) have weights $3/10$, $3/10$, and -1. Their cycle sum is $-2/5$, an explicit rational witness that no shared potentials can explain the ranking.

A.3 A MEASURABLE CONSISTENT SELECTOR

For continuous unsigned queries, exact mirror ties have probability zero for fixed u. Set $s_i = \mathrm{sign}(u^\top x_i)$ from the observed mirror orders and $\ell = \sum_i s_i x_i$. Then $\ell^\top u = \sum_i |u^\top x_i| > 0$ almost surely. Maximize $\ell^\top v$ over $G \cap \{\|v\| \leq 1\}$. A maximum exists by compactness and is positive. It has unit norm, since otherwise positive scaling in the cone improves it. The gradient maximizer is unique. Two distinct unit maximizers have a midpoint of norm less than one, which can again be scaled to improve the objective. Its nuisance witness need not be unique.

For each finite order pattern, the graph of this unique optimizer is semialgebraic in the query coordinates. Feasibility and optimality can be expressed using finitely many polynomial inequalities and quantified real variables. It is consequently measurable. Arbitrary finite definitions on null or unreachable histories make the algorithm total. The same whole-cell conclusion applies to any other measurable consistent selector, including a properly defined analytic-center gradient direction.

B PROOF OF WHOLE-CELL LOCALIZATION

The argument has three components: regularity of the query distribution, endpoint-disjoint witnesses in two sampling regimes, and a margin-net argument. Both sampling regimes below concern the uniform one-round design of Theorem 2.

B.1 PROJECTION REGULARITY FOR UNIFORM QUERIES

The density and transverse-tail bounds below have absolute constants and use exact spherical normalization.

Lemma 4 (Central projections and transverse tails)**.** *Let $d \geq 3$, fix a unit u, and let W be uniform on $\mathbb{S}^{d-1}$. For $S = u^\top W$ with cumulative distribution function F, there are positive constants a_0, a_1, b_0, p_0 and $0 < q_0 \leq 1/8$ such that a central interval I contains all quantiles in $[1/2 - q_0, 1/2 + q_0]$, and the following bounds hold on I for every unit $w \perp u$:*

$$a_0\sqrt{d} \leq f_S(t) \leq a_1\sqrt{d}, \\ \mathbb{P}\{w^\top W \geq b_0/\sqrt{d} \mid S = t\} \geq p_0, \qquad \mathbb{P}\{w^\top W \leq -b_0/\sqrt{d} \mid S = t\} \geq p_0. \tag{15}$$

The conditional bounds refer to a density version.

Proof. A coordinate of a uniform sphere point has density

$$f_d(t) = c_d(1 - t^2)^{(d-3)/2}, \quad |t| < 1, \qquad c_d = \frac{\Gamma(d/2)}{\sqrt{\pi}\,\Gamma((d-1)/2)} \asymp \sqrt{d}. \tag{16}$$

On $I = [-1/(4\sqrt{d}), 1/(4\sqrt{d})]$ this density is bounded above and below by absolute multiples of $\sqrt{d}$, including $d = 3$. Symmetry and integration give a fixed central quantile interval. Conditional on

$S = t$, write $W = tu + \sqrt{1-t^2}V$, where V is uniform on the sphere in $u^\perp \simeq \mathbb{R}^{d-1}$. For unit w in that space,

$$\mathbb{E}(w^\top V)^2 = \frac{1}{d-1}, \qquad \mathbb{E}(w^\top V)^4 = \frac{3}{(d-1)(d+1)}.$$

Paley–Zygmund applied to $(w^\top V)^2$ gives a fixed positive probability of magnitude at least $1/\sqrt{2(d-1)}$. Central symmetry divides this probability equally between the two signs. Since $\sqrt{1-t^2}$ is bounded below on I, Equation (15) follows.

□

B.2 Separated witnesses from dependent rankings

Lemma 5 (Two-sided witness with fine and coverage regimes)**.** *Use the uniform query law and the projection and tail bounds of Lemma 4. Fix $0 < \eta \le 1$ and a unit alternative v with $\eta \le \theta = \operatorname{angle}(u, v) \le \pi/2$. For n independent unsigned queries, the probability that no pair satisfies*

$$u^\top(W_j - W_i) \ge a_*\eta/\sqrt{d}, \qquad v^\top(W_j - W_i) \le -b_*\eta/\sqrt{d} \tag{17}$$

is at most

$$Ce^{-cn} + C\exp\{-cn\min(n\eta, 1)\}. \tag{18}$$

The constants depend only on those in Lemma 4.

Proof. Write $v = \cos\theta\, u + \sin\theta\, w$, $w \perp u$, $\|w\| = 1$. Choose

$$q_* = \min\{a_0 b_0/16, q_0/8, 1/16\}, \qquad a_* = q_*/(2a_1), \qquad b_* = b_0/2.$$

A pair with both projections in I satisfies Equation (17) if

$$\frac{a_*\eta}{\sqrt{d}} \le S_j - S_i \le \frac{b_0\eta}{4\sqrt{d}}, \qquad w^\top W_i \ge \frac{b_0}{\sqrt{d}}, \qquad w^\top W_j \le -\frac{b_0}{\sqrt{d}}. \tag{19}$$

Indeed, $\sin\theta \ge 2\theta/\pi$ and $\theta \ge \eta$ give

$$v^\top(W_j - W_i) \le \frac{b_0\eta}{4\sqrt{d}} - \frac{2b_0\sin\theta}{\sqrt{d}} \le -\frac{b_0\eta}{2\sqrt{d}}.$$

Conditional on all projections, transverse coordinates of distinct endpoints are independent. An endpoint-disjoint matching selected using only the projections therefore supplies independent transverse success events, each of probability at least p_0^2.

Fine regime. Put $t = n\eta$ and first assume $t \le 2/q_*$. The probability transform $U_i = F(S_i)$ is uniform. Its order-statistic spacings have the representation

$$U_{(j+1)} - U_{(j)} = Z_{j+1}/T_n, \qquad T_n = \sum_{\ell=1}^{n+1} Z_\ell, \qquad Z_\ell \overset{\text{iid}}{\sim} \operatorname{Exp}(1) \tag{20}$$

(Pyke, 1965, Section 4.1). This representation can be realized by sampling the exponentials, inverting F for the ordered projections, drawing their independent conditional transverse components, and relabeling uniformly. Thus conditioning on all Z_ℓ preserves the transverse independence used here.

Choose every other adjacent pair between ranks $\lceil (1/2 - q_0/2)n \rceil$ and $\lfloor (1/2 + q_0/2)n \rfloor$. For n above a constant threshold this gives $M \ge q_0 n/4$ endpoint-disjoint pairs and distinct spacing exponentials. Let H be the event that these projections lie in I and $n/2 \le T_n \le 2n$. The central quantile margin in Lemma 4 and binomial Chernoff bounds put all these ranks in I except with probability Ce^{-cn}. Exponential Chernoff bounds control both tails of T_n, so $\mathbb{P}(H^c) \le Ce^{-cn}$.

For a selected spacing, require $q_* t \le Z_{j+1} \le 2q_* t$. On H, integrating both density bounds gives

$$\frac{Z_{j+1}}{2a_1 n\sqrt{d}} \le S_{(j+1)} - S_{(j)} \le \frac{2Z_{j+1}}{a_0 n\sqrt{d}}.$$

This exponential interval implies the gap bounds in Equation (19). Its probability is

$$p_t = e^{-q_* t} - e^{-2q_* t} \ge q_* t\, e^{-2q_* t} \ge q_* e^{-4} t.$$

Let J count selected exponentials in that interval. Conditional transverse independence bounds the probability of no witness on H by $(1-p_0^2)^J$. Removing the indicator of H in the upper bound and using independence of the selected exponentials before division by T_n gives

$$\begin{aligned}\mathbb{P}(\text{no witness}) &\le \mathbb{P}(H^c) + \mathbb{E}(1-p_0^2)^J \\ &\le Ce^{-cn} + (1-p_0^2 p_t)^M \le Ce^{-cn} + \exp(-cn^2\eta).\end{aligned}$$

No independence between H and J, or between normalized spacings, was used.

Coverage regime. Now $t \ge 2/q_*$. Put $p = q_*\eta$, so $np \ge 2$ and $p \le q_0/8$. Within $[1/2 - q_0, 1/2 + q_0]$, pack $K = \lfloor q_0/(2p) \rfloor \ge q_0/(4p)$ blocks of width $4p$. In a block starting at a_ℓ, use intervals

$$I_\ell^- = [a_\ell, a_\ell + p], \qquad I_\ell^+ = [a_\ell + 2p, a_\ell + 3p].$$

Match as many endpoints as possible between the two intervals, choosing matches deterministically by original indices. Every matched gap in probability coordinates lies between p and $3p$. The density bounds imply

$$\frac{q_*\eta}{a_1\sqrt{d}} \le S_j - S_i \le \frac{3q_*\eta}{a_0\sqrt{d}} \le \frac{b_0\eta}{4\sqrt{d}},$$

which implies the gap conditions in Equation (19). These are separated-block pairs, not adjacent pairs in the full ordering. Their true quantile positions are used only in the proof.

Let N_ℓ^-, N_ℓ^+ be the occupancy counts and $M = \sum_\ell \min(N_\ell^-, N_\ell^+)$. Multinomial moments give $\mathbb{E}N_\ell^\pm = np$ and $\mathbb{E}(N_\ell^- - N_\ell^+)^2 = 2np$, regardless of dependence across bins. Consequently,

$$\mathbb{E}\min(N_\ell^-, N_\ell^+) = np - \tfrac{1}{2}\mathbb{E}|N_\ell^- - N_\ell^+| \ge np - \sqrt{np/2} \ge np/2,$$

and $\mathbb{E}M \ge Knp/2 \ge q_0 n/8$. Replacing one independent U_i changes M by at most two. The exposure martingale therefore has conditional increment ranges of length at most two. Iterating Hoeffding's exponential-moment bound (Hoeffding, 1963, Eq. (4.16)) gives $\mathbb{P}(M - \mathbb{E}M \le -t) \le e^{-t^2/(2n)}$. Taking $t = q_0 n/16$ yields

$$\mathbb{P}(M < q_0 n/16) \le \exp(-q_0^2 n/512).$$

Conditional on all projections, each of these disjoint pairs has transverse success probability at least p_0^2. Hence

$$\mathbb{P}(\text{no witness}) \le e^{-q_0^2 n/512} + e^{-p_0^2 q_0 n/16} \le 2e^{-cn}.$$

Combining the regimes and enlarging C to cover bounded n establishes Equation (18). □

B.3 Whole-cell localization

B.3.1 Turning a separated witness into an observed inequality

For any actual nuisance vector with range at most τ, a pair satisfying the first part of Equation (17) and $\tau \le a_*\eta/(2\sqrt{d})$ has

$$s_{j,+} - s_{i,+} = u^\top(W_j - W_i) + (e_j - e_i) > 0, \qquad s_{j,-} - s_{i,-} = -u^\top(W_j - W_i) + (e_j - e_i) < 0.$$

Thus the observed ranking supplies a reverse-order halfspace excluding the witness alternative with a negative margin. Candidate potentials remain unrestricted. The witnessing event depends only on the fixed u and the query directions. On this event, the implication holds simultaneously for all actual nuisance values of the stated range. The target is fixed before the random design is drawn.

B.3.2 Proof of the global theorem

Take a deterministic Euclidean net of the sphere with mesh $\zeta = c_{\text{net}}\varepsilon/\sqrt{d}$ and at most $(C\sqrt{d}/\varepsilon)^d$ points. Choose c_{net} sufficiently small relative to a_*, b_*. A feasible direction farther than ε from u has a nearest net point separated by at least $\varepsilon/2$. For net points at angle at most $\pi/2$, apply Lemma 5 with $\eta = \varepsilon/2$. Taking $\tau \le a_*\varepsilon/(4\sqrt{d})$ makes the true gap enforce a reverse-order relation. The alternative margin is at most $-b_*\varepsilon/(2\sqrt{d})$. Replacing the net point by the original candidate changes the inner product with $W_j - W_i$ by at most 2ζ, so the same relation excludes that candidate.

For larger angles, use disjoint independent pairs of uniform endpoints. Their difference D is rotationally invariant. Its direction is uniform and independent of its length, and $\mathbb{P}(\|D\| \geq 1) \geq 1/2$. For a uniform direction V, let Z be its projection length onto a plane containing u and the alternative v_0. Spherical moments give $\mathbb{E}Z^2 = 2/d$ and $\mathbb{E}Z^4 = 8/(d(d+2))$. Thus $\mathbb{P}(Z \geq 1/\sqrt{d}) \geq 1/8$. Independently of Z, the polar angle is uniform. If $\mathrm{angle}(u, v_0) \geq \pi/3$, a polar interval of half-width $1/8$ about $(u - v_0)/\|u - v_0\|$ gives

$$u^\top D \geq 1/(4\sqrt{d}), \qquad v_0^\top D \leq -1/(4\sqrt{d})$$

whenever $Z \geq 1/\sqrt{d}$ and $\|D\| \geq 1$. For antipodal u, v_0, choose any plane through their line. This event has probability bounded below by an absolute positive constant. The inequality survives the nuisance and net perturbations after reducing the constants. The probability that these independent pairs yield no witness is at most Ce^{-cn}.

A union bound over the net gives

$$\mathbb{P}\{\mathcal{C}_{\mathrm{rev}} \not\subseteq \mathcal{B}(u, \varepsilon)\} \leq C(C\sqrt{d}/\varepsilon)^d \left[e^{-cn} + e^{-cn\min(n\varepsilon,1)}\right]. \tag{21}$$

The two requirements $n \geq CL_\varepsilon$ and $n^2\varepsilon \geq CL_\varepsilon$ make this at most δ. They follow from Equation (8). Together with Equation (6), this establishes Theorem 2.

B.3.3 Graceful degradation and the continuing value of mirrors

Let c be small enough for Theorem 2 and set $\varepsilon_{\mathrm{out}} = \max\{\varepsilon, c^{-1}\sqrt{d}\,\tau\} \leq 1/10$. The sample requirement in Equation (8) decreases as its precision argument increases, so the sample size for ε also suffices for $\varepsilon_{\mathrm{out}}$. Applying the theorem at $\varepsilon_{\mathrm{out}}$ gives $\mathcal{C}_{\mathrm{rev}} \subseteq \mathcal{B}(u, \varepsilon_{\mathrm{out}})$ with probability at least $1 - \delta$.

This is not a minimax accuracy floor. For any even nuisance, a mirror sign is $\mathrm{sign}(u^\top W)$. Against an alternative at angle θ, a uniform query has, with probability at least $c\theta$, opposite projections of magnitude at least $c\theta/\sqrt{d}$. Project onto the target–alternative plane, require planar radius at least $1/\sqrt{d}$, and choose a subwedge centered at $(u - v)/\|u - v\|$. Its angular width is a constant multiple of θ. A margin net then gives whole-cell recovery from mirrors whenever

$$n \geq \frac{C}{\varepsilon}\left[d\log(C\sqrt{d}/\varepsilon) + \log(C/\delta)\right], \tag{22}$$

without any restriction on τ. Full enforces these constraints as well. The sharper adaptive minimax achievability is proved in Appendix D.2.

For a quadratic nuisance, the Rayleigh-quotient extrema give $\Omega_a(E) = a^2(\lambda_{\max}(H) - \lambda_{\min}(H))/2$, proving the expression following Equation (7). Isotropic curvature does not enter the fast condition.

C Lower Bounds in the Small-Variation Regime

Proposition 6 (Known isotropic subclass)**.** *For $d \geq 3$, $0 < \varepsilon \leq 1/10$, and $R \geq 1$, every algorithm satisfying Equation* (2) *on $q_u(x) = u^\top x + \|x\|^2/2$, with the Hessian known, obeys the following bound, where $A_\varepsilon = (d-1)\log(1/\varepsilon)$:*

$$N \geq \max\left\{\frac{d\cos^2\varepsilon}{2},\ \sqrt{\frac{(d-1)R}{2e}(\varepsilon^{-1/R} - 1)},\ \frac{A_\varepsilon}{\log(2 + A_\varepsilon)}\right\}. \tag{23}$$

The algorithm may use cumulative orders, arbitrary radii, and adaptive batch sizes.

For $R = 1$, the middle term in Equation (23) is $\sqrt{(d-1)(\varepsilon^{-1} - 1)/(2e)}$, which gives the stated $\Omega(\sqrt{d/\varepsilon})$ contribution.

Proof. Draw u uniformly and fix a seed. As in Appendix D.1, unfold the finite tree. Nontrivial equality sets have zero spherical measure. Repeats add no partition. With $D = d - 1$, the number of regions formed on $\mathbb{S}^{d-1}$ by $m \geq 1$ affine hyperplanes is at most $2\sum_{j=0}^{D}\binom{m-1}{j} \leq (1+2em/D)^D$. To

see the first estimate, successively add a hyperplane and count the regions induced on its intersection sphere. The circle base case has at most $2m$ arcs. Empty, coincident, and tangent intersections only reduce the count. The binomial estimate is as in Equation (26). Set the count to one for $m = 0$.

A round with p old endpoints and n new endpoints has at most $pn + \binom{n}{2} \le Nn$ new pairwise equalities. Each is an affine hyperplane in u, even for different physical radii. The remaining-budget recursion therefore bounds the number of leaves by

$$\max_{\sum n_r \le N} \prod_{r=1}^{R} (1 + 2eNn_r/D)^D \le (1 + 2eN^2/(DR))^{DR}.$$

The cap bound from Appendix D.1 gives average success at most $\varepsilon^D(1 + 2eN^2/(DR))^{DR}/2$. Integrating over the independent seed and imposing average success at least $3/4$ establishes the square-root term in Equation (23).

For the dimension term, give the algorithm the stronger oracle of exact numerical values of the known quadratic and allow adaptation after every endpoint. This supplies exact linear measurements of u. It suffices to treat $N < d$. Orthogonalizing and adding unused measurements when needed can only increase information, so the stronger transcript contains N adaptively chosen orthonormal coordinates. Conditional on their values and the seed, the remaining component is uniform on a sphere in the unmeasured subspace. If v_N is the measured projection and $r^2 = 1 - \|v_N\|^2$, reflection of the residual pairs two equally probable targets separated by angle $2 \arcsin r$. When $r > \sin \varepsilon$, no one estimate is accurate for both.

The conditional expected square of measurement $j + 1$ is $(1 - \|v_j\|^2)/(d - j)$. Induction gives $\mathbb{E}\,\|v_N\|^2 = N/d$ under adaptive selection. Consequently

$$\mathbb{P}(\text{success}) \le \tfrac{1}{2} + \tfrac{1}{2}\mathbb{P}(\|v_N\|^2 \ge \cos^2 \varepsilon) \le \tfrac{1}{2} + \frac{N}{2d \cos^2 \varepsilon}.$$

Success probability $3/4$ requires $N \ge d \cos^2 \varepsilon/2$, also immediate for $N \ge d$. This applies a fortiori to rankings.

For the last term, fix a seed and label endpoints by evaluation order, using a fixed order within each batch. Pad stopped histories to N labels. Outside the null equality sets of the finite tree, distinct transcript leaves induce distinct final permutations. Indeed, at their first differing feedback the queried points coincide and their prefix orders differ. Restriction of a common final permutation could not recover both. Identical-point ties are deterministic at that node and can be broken by label for this counting argument. Thus there are at most $N!$ leaves, even with fully sequential feedback. The same cap bound gives average success at most $N!\varepsilon^{d-1}/2$. Averaging over seeds and using $3/4$ success yields $\log(N!) \ge A_\varepsilon + \log(3/2)$, hence $N \log N \ge A_\varepsilon$. If $N < A_\varepsilon$, this implies $N > A_\varepsilon / \log(2 + A_\varepsilon)$. If $N \ge A_\varepsilon$, the displayed bound is immediate. □

In one round the bound is $\Omega(d + \sqrt{d/\varepsilon})$. Every shell-variation class considered in Theorem 2 contains this zero-variation subclass. The permutation bound also prevents unlimited feedback from removing precision dependence altogether.

Corollary 7 (One-round Mirror lower bound)**.** *Let $d \ge 3$ and $0 < \varepsilon \le 1/10$. Any one-round procedure whose feedback consists only of antipodal signs and which satisfies Equation* (2) *on the known isotropic family $q_u(x) = u^\top x + \|x\|^2/2$ must use*

$$N \ge \frac{d-1}{2e}\left[(3/2)^{1/(d-1)}\varepsilon^{-1} - 1\right] = \Omega(d/\varepsilon) \tag{24}$$

endpoints. The same lower bound applies to every favorable class that contains this zero-variation family.

Proof. Fix the private seed and draw u uniformly on $\mathbb{S}^{d-1}$. A one-round transcript with at most N antipodal signs partitions the sphere with at most $C(N, d)$ homogeneous sign regions, where C is defined in Equation (26). One output is associated with each region. The cap bound in Appendix D.1 therefore limits the conditional success probability to $\varepsilon^{d-1}C(N, d)/2$. Requiring average success of at least $3/4$ and using Equation (26) gives Equation (24). Averaging over the private seed preserves the inequality, so failure below this budget occurs for at least one fixed u. The isotropic nuisance has $\tau = 0$ on every shell. □

D THE UNBOUNDED-SCALE ENDPOINT–ROUND BARRIER

The lower bound permits full cumulative rankings. The matching construction uses only mirror signs and therefore also works with separate batch rankings and arbitrary even nuisance.

D.1 THE CUMULATIVE-RANKING LOWER BOUND

D.1.1 A FINITE TREE BEFORE CHOOSING AN INSTANCE

Fix an algorithm with hard budgets N, R and include all randomization, including decoding, in its private seed ω. Each weak ordering of at most N endpoint labels belongs to a finite alphabet. For a fixed seed, unfolding every possible ordinal history through R rounds therefore gives a finite tree. Pad stopped histories with empty rounds and use finite dummy queries on unreachable histories, enforcing the same hard budget. Let $\mathcal{X}(\omega)$ be the finite set of points appearing anywhere in this tree. It depends on the algorithm and seed, not on its subsequently chosen instance.

Fix $\kappa > 1$ and put $\delta_\kappa = (\kappa - 1)/(2(\kappa + 1)) \in (0, 1/2)$. Independently draw $A = I + S$, with S absolutely continuously distributed on the symmetric Frobenius ball $\|S\|_F < \delta_\kappa$. Then

$$\operatorname{cond}(A) < \frac{1 + \delta_\kappa}{1 - \delta_\kappa} = \frac{3\kappa + 1}{\kappa + 3} < \kappa.$$

For fixed ω and $xx^\top \neq yy^\top$, the equality $\operatorname{tr}(A(xx^\top - yy^\top)) = 0$ is a proper affine hyperplane in the symmetric matrix variable. It has measure zero. Taking the finite union over tree pairs and integrating over the seed shows that

$$D(\omega, A) = \max_{\substack{x,y \in \mathcal{X}(\omega) \\ xx^\top \neq yy^\top}} \frac{2\,\|x - y\|}{|\operatorname{tr}(A(xx^\top - yy^\top))|} \tag{25}$$

is measurable and almost surely finite, with an empty maximum equal to zero.

Choose one deterministic $t > 0$ such that $\mathbb{P}_{\omega,A}(D \geq t) \leq 1/8$. Draw u independently and uniformly on $\mathbb{S}^{d-1}$ and set $q(x) = u^\top x + (t/2)x^\top Ax$. The multiplier may depend on the prescribed algorithm, budgets, and κ, but not on the realized seed, matrix, or target. No moment bound on D is required. This is a distribution on fixed instances in $\mathcal{Q}_{d,\kappa}$.

On $\mathcal{G} = \{D < t\}$, every distinct-projector pair anywhere in the tree obeys

$$\left|\frac{t}{2}\operatorname{tr}(A(xx^\top - yy^\top))\right| > \|x - y\| \geq |u^\top(x - y)|$$

simultaneously for all unit u. Its score order is fixed by A. If $xx^\top = yy^\top$, then $y = x$ or $y = -x$ (including the zero case). Repeats are fixed ties. A nonzero antipode contributes only $\operatorname{sign}(u^\top x)$. For a uniform u, directional ties have probability zero after a finite union over the tree. For fixed $(\omega, A) \in \mathcal{G}$, all remaining gradient information is consequently a tree of homogeneous sign tests.

At a node adding n endpoints, at most n previously unknown antipodal signs become available. Each newly completed equal-projector class requires at least one new endpoint, but its opposite endpoint may have been evaluated in an earlier round. This explains why a count of $n/2$ would be incorrect for cumulative rankings.

D.1.2 ARRANGEMENTS WITH HISTORY-DEPENDENT BATCH SIZES

Put $D = d - 1$. The number of strict spherical regions formed by $n \geq 1$ homogeneous hyperplanes in $\mathbb{R}^d$ is at most

$$C(n, d) = 2\sum_{j=0}^{d-1} \binom{n-1}{j} \leq (1 + 2en/D)^D, \qquad C(0, d) = 1. \tag{26}$$

The combinatorial formula follows by adding one hyperplane and counting the regions induced on it by its predecessors, with the one-dimensional and one-hyperplane base cases. For $1 \leq n \leq D$, use $2^n \leq (1 + n/D)^D$. For $n \geq D + 1$, the binomial bound $\sum_{j=0}^{D} \binom{n-1}{j} \leq (e(n-1)/D)^D$ follows by

setting $z = D/(n-1) \le 1$ in $z^D \sum_{j \le D} \binom{n-1}{j} \le (1+z)^{n-1} \le e^D$. These inequalities establish the displayed estimate. Restricting to a previous history does not increase the number of regions.

Let $L(N, R)$ bound the leaves of a sign tree with remaining budgets N, R. At a node with n new endpoints, each of at most $C(n, d)$ children has at most $L(N-n, R-1)$ leaves. Induction yields

$$L(N,R) \le \max_{n_1+\cdots+n_R \le N} \prod_{r=1}^{R} C(n_r, d) \le (1 + 2eN/(DR))^{DR}.$$

The final step uses concavity of $\log(1 + 2ex/D)$. The maximizing sequence is an upper bound on all subtrees, not an assumption that the actual algorithm fixes its allocation in advance. Empty rounds allow stopping.

D.1.3 Cap coverage and randomized fixed-instance quantifiers

The normalized measure of an angular ε-cap on $\mathbb{S}^{d-1}$ is at most $\varepsilon^D/2$. Indeed,

$$\frac{\int_0^\varepsilon \sin^{D-1} t \, dt}{\int_0^\pi \sin^{D-1} t \, dt} \le \frac{\varepsilon^D/D}{2/D},$$

using $\sin t \le t$ in the numerator. For the denominator, symmetry and $\cos t \le 1$ on $[0, \pi/2]$ give

$$\int_0^\pi \sin^{D-1} t \, dt = 2 \int_0^{\pi/2} \sin^{D-1} t \, dt \ge 2 \int_0^{\pi/2} \sin^{D-1} t \cos t \, dt = \frac{2}{D}.$$

For fixed $(\omega, A) \in \mathcal{G}$, there is one output per leaf. A union bound on its possible success caps gives conditional success probability at most $\varepsilon^D L(N, R)/2$.

The event $\mathcal{G}$ involves only ω, A, so u is still uniform and independent after conditioning. Allowing success probability one on its complement gives

$$\mathbb{P}(\text{success}) \le \tfrac{1}{8} + \tfrac{1}{2}\varepsilon^D (1 + 2eN/(DR))^{DR}.$$

If Equation (2) holds on every fixed member of $\mathcal{Q}_{d,\kappa}$, it holds on average under the independent instance distribution. Hence

$$N \ge \frac{DR}{2e} \left[(5/4)^{1/(DR)} \varepsilon^{-1/R} - 1 \right] \ge \frac{DR}{2e} (\varepsilon^{-1/R} - 1). \tag{27}$$

Violating this bound therefore forces failure on at least one fixed quadratic. Shrinking the open matrix support as $\kappa \downarrow 1$ changes the quantile t, but no constant in the arrangement or cap argument. This establishes the uniformity claimed in Theorem 3.

D.2 A finite Mirror construction for matching achievability

The construction in this section supplies the upper half of Theorem 3. It uses only the identity $f(aw) - f(-aw) = 2a \, \|g\| \, u^\top w$ and thus works for arbitrary even nuisance.

D.2.1 First-round ratio information and subsequent refinement

Draw a Haar-distributed orthonormal basis $(a_1, \ldots, a_d)$ and write $G_i = u^\top a_i$. Choose subdivisions $M_1, \ldots, M_s \ge 2$, where $s \le R$ and M_1 is even. In the first batch, query mirrors of all d axes. On every edge (i, j) with $i \in \{1, 2, 3\}$ and $i < j \le d$, also query both lines

$$\cos\theta \, a_i + \sin\theta \, a_j, \qquad \sin\theta \, a_i - \cos\theta \, a_j, \quad \theta = \frac{\ell\pi}{2M_1}, \quad 1 \le \ell < M_1. \tag{28}$$

There are $3d - 6$ edges. The grid includes $\pi/4$, so after feedback the three candidate edges determine $h = \arg\max_{i \le 3} |G_i|$. All edges incident to this selected coordinate have already been queried in the same batch.

For each $i \ne h$, let $\psi_i = \arctan(G_i/G_h) \in (-\pi/2, \pi/2)$. Axis signs give its half-domain. To check the grid information, orient an edge temporarily as (j, i) and write $\phi = \arctan(|G_i|/|G_j|)$.

If the two coordinate signs agree, the second line in Equation (28) compares ϕ with θ. Otherwise the first compares it with $\pi/2 - \theta$. Reversing the stored edge exchanges ϕ and $\pi/2 - \phi$. These reflections preserve the grid. Thus each selected signed interval has width $\pi/(2M_1)$, with no separate initialization round.

In round $r \geq 2$, subdivide each retained interval into M_r equal cells. At every internal threshold θ, query mirrors of $z_{i,\theta} = \cos\theta\, a_i - \sin\theta\, a_h$. With $s_h = \operatorname{sign}(G_h)$,

$$s_h u^\top z_{i,\theta} = \frac{|G_h|}{\cos\psi_i} \sin(\psi_i - \theta),$$

so its sign identifies the correct subinterval. With $Q = \prod_{r=1}^{s} M_r$, the final width is $\Delta = \pi/(2Q)$. For signed midpoints m_i, return the normalization of $s_h(a_h + \sum_{i \neq h} \tan m_i\, a_i)$. All coordinate zeros and the finitely many threshold equalities have probability zero under the Haar basis. Assigning arbitrary finite outputs on such exceptional histories defines a total algorithm without changing the conclusion. The paid cost is

$$N = 2d + 4(3d-6)(M_1 - 1) + 2(d-1)\sum_{r=2}^{s}(M_r - 1). \tag{29}$$

D.2.2 Risk of the actual finite midpoint decoder

For a uniform partition of $[0, \pi/2]$ with width Δ, let m be the midpoint of the cell containing $\phi < \pi/2$. Then

$$|\tan m - \tan\phi| \leq \Delta(1 + \tan^2\phi). \tag{30}$$

To verify this even in the last cell, use $|m - \phi| \leq \Delta/2$, $m \leq \pi/2 - \Delta/2$, and $\cos\phi \leq \cos m + \sin m \sin(\Delta/2) \leq 2\cos m$. The tangent difference identity then gives $|\tan m - \tan\phi| = |\sin(m - \phi)|/(\cos m \cos\phi) \leq \Delta/\cos^2\phi$.

Reflect signed cells onto their absolute half-domain and apply Equation (30). In basis coordinates, use $v_h = G_h$ and $v_i = G_h \tan m_i$ for analysis only. Normalizing this vector is exactly the implemented decoder. The coordinate error obeys

$$\|v - G\|^2 \leq 2\Delta^2 \left((d-1)G_h^2 + \sum_{i \neq h} \frac{G_i^4}{G_h^2} \right). \tag{31}$$

Write $G = Z/\|Z\|$ with independent standard Gaussian coordinates and $M = \max_{j \leq 3} |Z_j|$. The first term in parentheses has expectation at most 3. The two unselected candidate coordinates contribute at most 1. For $p = d - 3 > 0$ and $S = \sum_{i=4}^{d} Z_i^2$,

$$\sum_{i=4}^{d} \frac{G_i^4}{G_h^2} \leq \frac{1}{M^2} \frac{\sum_{i=4}^{d} Z_i^4}{S}.$$

The two factors are independent. Since $M^2 \geq (Z_1^2 + Z_2^2 + Z_3^2)/3$, the first expectation is at most $3\mathbb{E}[(\chi_3^2)^{-1}] = 3$. Gaussian radial decomposition gives the second expectation $3p/(p+2) \leq 3$. When $p = 0$ its contribution is absent. Thus the bracket expectation is at most $3 + 1 + 9 = 13$, with no assumption that the selected hub is independent of normalized coordinates.

The reverse triangle inequality and the unit chord formula imply $\operatorname{angle}(v/\|v\|, G) \leq \pi\|v - G\|$, so the actual finite decoder satisfies

$$\mathbb{E}\operatorname{angle}(\widehat{u}, u)^2 \leq 26\pi^2\Delta^2 = \frac{26\pi^4}{4Q^2}. \tag{32}$$

D.2.3 Uniform optimization over a round cap

Set $K_0 = \pi^2\sqrt{26}$, $a_\varepsilon = \log(1/\varepsilon)$, and $s = \min\{R, \lceil a_\varepsilon \rceil\}$. Choose all $M_r = M$, the least even integer at least $(K_0/\varepsilon)^{1/s}$. Then $Q \geq K_0/\varepsilon$ and Equation (32) is at most $\varepsilon^2/4$. Markov's inequality gives Equation (2). The cost is at most $12dsM \leq Cds\varepsilon^{-1/s}$. If $R \leq a_\varepsilon$, then $s = R$ and $\varepsilon^{-1/R} \geq e$, yielding $CdR(\varepsilon^{-1/R} - 1)$. If $R > a_\varepsilon$, then $s = \lceil a_\varepsilon \rceil$ and the cost is $O(da_\varepsilon)$. Use $R(e^{a_\varepsilon/R} - 1) \geq a_\varepsilon$. This establishes the matching upper bound uniformly over R and κ.

E Model Error, Ambiguity, and Valid Retention

E.1 Calibrated localization: formal statements

On a fixed shell, write the observed normalized scores as $e_i \pm (u^\top W_i + o_i)$, with $|o_i| \le \rho$ and actual even-offset range at most τ_a. The shared-error cell $\mathcal{C}_\rho$ consists of unit candidates v for which free even offsets e'_i and shared $b_i \in [-\rho, \rho]$ explain the ranking as $e'_i \pm (v^\top W_i + b_i)$. Take d, ε, δ and the uniform query design as in Theorem 2.

Corollary 8 (Bounded shared-error localization)**.** *The true direction belongs to $\mathcal{C}_\rho$. The endpoint count of Theorem 2 gives $\mathcal{C}_\rho \subseteq \mathcal{B}(u, \varepsilon)$ with probability at least $1 - \delta$ whenever $\tau_a + \rho \le c\varepsilon/\sqrt{d}$, for a sufficiently small universal c.*

Corollary 9 (Fixed-center recovery with a known smoothness scale)**.** *Take d, ε, δ as in Theorem 2. Suppose ∇f is L-Lipschitz on the Euclidean ball $\{x : \|x\| \le a_0\}$, $L > 0$, and $\|\nabla f(0)\| \ge g_{\min} > 0$. For a sufficiently small universal $c_0 > 0$, choose*

$$0 < a \le \min\{a_0, c_0 \varepsilon g_{\min}/(L\sqrt{d})\}, \qquad \rho = La/(2g_{\min}).$$

Under exact score rankings, the shared-error model on $\{\pm aW_i\}$ contains the true gradient direction and satisfies the whole-cell conclusion and endpoint-complexity rate of Theorem 2. Exact evenness and a third-derivative bound are unnecessary.

E.2 Why an exact-even fit can fail outside its model

Proposition 10 (Single-shell ambiguity under an odd remainder)**.** *Let u, q be orthogonal unit vectors, $a > 0$, $\mu \ne 0$, and E a differentiable even function. The objectives*

$$f_\mu(x) = u^\top x + E(x) + \mu(q^\top x)\|x\|^2, \qquad \widetilde{f}_a(x) = (u + \mu a^2 q)^\top x + E(x) \tag{33}$$

coincide on $\|x\| = a$, but their gradient directions at zero differ by $\Delta = \arctan(|\mu| a^2)$. Any randomized ordinal procedure restricted to this sphere has angular error at most $\varepsilon < \Delta/2$ with probability at most $1/2$ on at least one of these two instances.

Proof. On the sphere, $\|x\|^2 = a^2$. The even term and cubic term have zero gradient at the origin, giving the stated directions and angle. Identical values imply identical transcript and output distributions, even for adaptive queries. The two angular success caps are disjoint, so their probabilities sum to at most one. □

Thus a valid certificate for the fitted direction set need not cover the true gradient outside the even-nuisance model. Shrinking the physical radius reduces this cubic bias, but retention is monotone under the add-only rule. If $u \notin \mathcal{C}_1$, then $u \notin \mathcal{C}_r \subseteq \mathcal{C}_1$. Restoring validity in that case requires changing the model or discarding invalid constraints.

E.3 A full shared-error model and its localization result

At the fixed center, consider

$$f(x) = b + g^\top x + E(x) + O(x), \qquad E(-x) = E(x), \quad O(-x) = -O(x), \quad \nabla O(0) = 0.$$

Thus g remains the gradient at zero. On a radius-a shell, let $\rho_a = \sup_{\|w\|=1} |O(aw)|/(a\|g\|)$ and suppose a supplied envelope $\rho \ge \rho_a$ is available. Normalization gives the score model and shared-error cell $\mathcal{C}_\rho$ defined in Appendix E.1. Independent ranking-edge allowances would instead define a generally larger model.

Proof of Corollary 8. The true u, actual potentials, and actual odd values form a feasible witness. Consider $D = W_j - W_i$. If

$$u^\top D > \tau_a + 2\rho,$$

then the positive scores increase from i to j and the negative scores decrease. Both inequalities hold irrespective of the allowed even and odd values. Adding the corresponding inequalities for any feasible candidate cancels $e'_j - e'_i$ and gives

$$v^\top D \geq b_i - b_j \geq -2\rho. \tag{34}$$

Hence a pair satisfying $u^\top D > \tau_a + 2\rho$ and $v^\top D < -2\rho$ excludes v from the Full shared-error model.

Use the separated-witness event of Appendices B.2 and B.3, reserving a fixed fraction of its two margins for perturbations. For candidates at angular distance at least ε, that event supplies positive and negative margins of order $\varepsilon/\sqrt{d}$. The fine-spacing and coverage-block arguments give their stated common failure bound before any nuisance or error values are chosen. Taking $\tau_a + \rho \leq c\varepsilon/\sqrt{d}$ with c smaller than both reserved margin constants makes the first inequality strict and the candidate inequality incompatible with Equation (34). The same finite net and its margin allowance then exclude all far candidates simultaneously. Increasing the universal sample constant absorbs the fixed margin reduction without changing the endpoint-complexity rate.

No independence among ranking edges or among bounded errors is used. □

More generally, let the actual odd envelope be ρ_{true} and the fitted envelope be $\rho_{\mathrm{fit}} \geq \rho_{\mathrm{true}}$. The forcing margin is $\tau_a + 2\rho_{\mathrm{true}}$ and the exclusion margin is $2\rho_{\mathrm{fit}}$. The proof therefore gives the same count under $\tau_a + \rho_{\mathrm{true}} + \rho_{\mathrm{fit}} \leq c\varepsilon/\sqrt{d}$. At a nominal resolution ε, applying this result at $\max\{\varepsilon, C\sqrt{d}(\tau_a + \rho_{\mathrm{true}} + \rho_{\mathrm{fit}})\}$ gives graceful degradation whenever that radius is at most $1/10$. This sufficient localization scale need not be an accuracy floor. The cubic ambiguity in Proposition 10 supplies an instance-specific obstruction of order ρ_a.

For several physical shells, use physical budgets ω_i for normalized scores $e_i \pm (u^\top x_i + b_i)$, so $|b_i| \leq \omega_i$. A radius-a shell has normalized envelope $\max_i \omega_i/a$. If all budgets are valid and all shared variables are retained, the full unit-direction sets are nested and contain the same u. Large but valid old error budgets do not create the exclusion mechanism of Proposition 10.

A measurable consistent selector exists. Bound the potential gauges as in Appendix F.5 and take the lexicographically first unit direction in the compact feasible projection. Successive coordinate minima have semialgebraic graphs for each finite order pattern. For an implemented chart with $c/\|h\| \geq 1/2$, Equation (43) enlarges the fitted envelope by at most two, absorbed by the same one-round localization constants.

Proposition 11 (Resolution of a robust uniform-query cell)**.** *Fix a unit u, $n \geq 1$, $d \geq 3$, $\rho > 0$, and $0 < \delta < 1$. For n independent uniform query directions, observe the noiseless linear scores $\pm u^\top W_i$ and fit $\mathcal{C}_\rho$. With probability at least $1 - \delta$, its enclosing angular radius about any center is at least*

$$\frac{1}{2}\min\left\{1, \rho\sqrt{\frac{d}{2\log(2n/\delta)}}\right\}.$$

Proof. Write $\Delta = \min\{1, \rho\sqrt{d/[2\log(2n/\delta)]}\}$. Fix a unit v with $\|v - u\| = \Delta$ before drawing the queries. For unit z, the sphere moments satisfy $\mathbb{E}(z^\top W)^{2k} = (2k-1)!!/[d(d+2)\cdots(d+2k-2)] \leq (2k-1)!!/d^k$. The moment generating function is therefore at most $\exp(t^2/(2d))$, giving $\mathbb{P}\{|z^\top W| > t\} \leq 2\exp(-dt^2/2)$. Take $z = (u - v)/\Delta$ and union-bound the n projections. With probability at least $1 - \delta$, every $b_i = (u - v)^\top W_i$ has magnitude at most ρ. The candidate scores $\pm(v^\top W_i + b_i)$ then equal all observed scores exactly, so both u and v belong to $\mathcal{C}_\rho$. Their angular separation is $2\arcsin(\Delta/2) \geq \Delta$. The triangle inequality gives the radius bound. □

This is a finite-design whole-cell statement for the uniform query law, not a minimax lower bound against all adaptive designs. It shows why the $\sqrt{d}\,\rho$ resolution term cannot generally be removed from this shared-error cell analysis, up to logarithms, even when the actual instance has zero odd error.

E.4 From score noise and local smoothness to an error envelope

Suppose each stored endpoint score has error $\xi_{i,\pm}$ satisfying $|\xi_{i,\pm}| \le \nu$. On a radius-a shell, set $\zeta = \nu/(a\,\|g\|)$ and split the normalized errors as

$$\bar{\xi}_i = \frac{\xi_{i,+} + \xi_{i,-}}{2a\,\|g\|}, \qquad \widetilde{\xi}_i = \frac{\xi_{i,+} - \xi_{i,-}}{2a\,\|g\|}.$$

The first term is absorbed by the free even potentials and increases their range by at most 2ζ. The second is shared with opposite signs and has magnitude at most ζ. Thus a fitted odd envelope $\rho \ge \rho_a + \zeta$ is valid, and the sufficient localization condition becomes $\tau_a + 2\zeta + \rho \le c\varepsilon/\sqrt{d}$. The observed ranking is the total order of these stored noisy scores. This covers stochastic score perturbations while preserving transitivity. It does not model arbitrary cyclic pairwise judgments or partial rankings.

For a horizon of at most N evaluations, conditionally σ-sub-Gaussian score errors satisfy

$$\max_{j \le N} |\xi_j| \le \sigma\sqrt{2\log(2N/\delta_0)}$$

with probability at least $1 - \delta_0$, by conditional tail bounds and a union bound. Applying the bounded-error result on this event gives failure probability at most $\delta + \delta_0$, including adaptive query locations. Reusing a stored endpoint retains its realized noisy score. These error contracts refer to a calibrated score scale. An arbitrary unknown monotone link need not preserve their numerical size.

For a thrice differentiable objective with $\sup_{\|x\| \le a} \left\|D^3 f(x)\right\|_{\mathrm{op}} \le M_3$, define $E(x) = [f(x) + f(-x)]/2$ and $O(x) = [f(x) - f(-x)]/2 - g^\top x$, absorbing the constant into E. Taylor's integral remainder gives $|O(aw)| \le M_3 a^3/6$. A known lower bound $\|g\| \ge g_{\min} > 0$ therefore supplies the usable envelope

$$\rho \;=\; \frac{M_3 a^2}{6 g_{\min}} + \frac{\nu}{a g_{\min}}.$$

The two terms have opposite radius dependence. The even shell-variation condition remains separate. A third-derivative bound does not bound the anisotropic Hessian scale. The argument is at one fixed center and does not transfer retained constraints to a changing gradient.

Proof of Corollary 9. Set $g = \nabla f(0)$ and write the first-order remainder as $r(x) = f(x) - f(0) - g^\top x$. Smoothness gives $|r(\pm aw)| \le La^2/2$. Its even and odd parts $E(x) = [r(x) + r(-x)]/2$ and $O(x) = [r(x) - r(-x)]/2$ satisfy $\Omega_a(E) \le La^2$ and $|O(aw)| \le La^2/2$. Thus $\tau_a \le La/g_{\min}$ and $\rho_a \le \rho$. Taking c_0 small enough in Corollary 8 establishes the result. □

The scale inputs are supplied rather than inferred from ordinal feedback, as in calibrated comparison-based recovery (Tao et al., 2026). The unknown-curvature hard class has no common finite L, so this consequence does not circumvent its uniform-budget barrier. With score error ν, the sufficient condition instead includes $\nu/(ag_{\min})$, making arbitrarily small physical radii unsuitable.

F Fitting and Certifying the Direction Set

The certificate encloses a projection of the fitted model. Its basic support inequality is

$$c^\top v \le \alpha + M\left\|c + A^\top\lambda - \alpha\ell\right\|_1, \tag{35}$$

valid on a section with $Av \ge 0$, $\ell^\top v = 1$, $\|v\|_\infty \le M$, and any $\lambda \ge 0$. The section bound and residual-checked angular enclosure follow below.

F.1 A bounded section in gradient variables

Let X have the unsigned stored query vectors as rows, and assume they span $\mathbb{R}^d$. Let s_i be their exact observed Mirror signs, A contain the Mirror and valid reverse-order rows, and $G_{\mathrm{rev}} = \{v : Av \ge 0\}$. It contains the Full direction cell. Define $\ell = X^\top s$. For every nonzero $v \in G_{\mathrm{rev}}$,

$$\ell^\top v = \sum_i s_i (Xv)_i > 0.$$

The summands are nonnegative, and a zero sum would imply $Xv = 0$, contradicting full column rank. Every feasible ray therefore intersects $\ell^\top v = 1$. On this section, $\|Xv\|_\infty \le 1$ because each nonnegative mirror projection is bounded by their sum.

Suppose L is a proposed left inverse with the exactly checked induced norm $q = \|I - LX\|_\infty < 1$. Then

$$\|v\|_\infty \le \|L\|_\infty \|Xv\|_\infty + q\|v\|_\infty, \qquad \|v\|_\infty \le M := \frac{\|L\|_\infty}{1-q}.$$

All quantities can be verified over the exact rationals represented by stored floating-point coordinates. The proposed inverse is used with its residual included in the bound. This bounds the gradient section independently of the nuisance potentials.

Proposition 12 (Residual-compensated support and angular bounds)**.** *Assume the preceding section bound. For any objective vector c, any $\lambda \ge 0$, and any real α, define*

$$U(c;\lambda,\alpha) = \alpha + M\left\|c + A^\top\lambda - \alpha\ell\right\|_1. \tag{36}$$

Then $c^\top v \le U(c;\lambda,\alpha)$ for every feasible section point. Let $h \ne 0$, $P = I - hh^\top/(h^\top h)$, and obtain coordinate intervals $l_i \le (Pv)_i \le u_i$ and a lower bound $h^\top v \ge p > 0$ from these supports. Then every feasible direction lies within angular radius

$$\beta = \min\left\{4, \frac{\|h\|\sqrt{\sum_i \max\{|l_i|,|u_i|\}^2}}{p}\right\} \tag{37}$$

of $h/\|h\|$, with outward rounding. If $p \le 0$ or a bounded section has not been established, the trivial radius 4 remains valid.

Proof. Write $r = c + A^\top\lambda - \alpha\ell$. On the section, $c^\top v = \alpha - \lambda^\top Av + r^\top v \le \alpha + M\|r\|_1$. Use objectives $P_{i,:}, -P_{i,:}$ for the intervals and $-h$ for the parallel lower bound. When $p > 0$, the angle is below $\pi/2$ and

$$\tan\operatorname{angle}(h,v) = \frac{\|h\|\,\|Pv\|}{h^\top v} \le \frac{\|h\|\sqrt{\sum_i \max\{|l_i|,|u_i|\}^2}}{p}.$$

Since $\operatorname{angle}(h,v) \le \tan\operatorname{angle}(h,v)$, Equation (37) follows. The radius $4 > \pi$ covers all cases. □

The numerical optimizer proposes multipliers and primal points. Rational arithmetic independently checks multiplier nonnegativity, matrix products, norm bounds, and residual allowances, without relying on solver-reported dual feasibility or exact stationarity. A sparsified multiplier proposal is admissible only with its recomputed residual. Positive square roots and the reported radius are rounded outward. This produces a certificate for all directions allowed by the stored-coordinate model, rather than a statement based on the measured error at the true target.

F.2 Transitive reduction and certificate completion

The reverse constraints can be represented as comparisons among signed linear projections. Their strictly observed ordering is acyclic. If a directed comparison has a path through other retained comparisons, summing the endpoint differences along the path recovers its row. Removing that edge therefore leaves the gradient cone unchanged. The implementation checks that every removed edge has a retained path. This reduction leaves the Full decoder unchanged.

Coordinate boxes need not give tight angular caps even when the underlying cone is small. We tighten them using the exact tangent identity $h^\top Pv = 0$. Whenever $h_i \ne 0$,

$$(Pv)_i = -\sum_{j\ne i}(h_j/h_i)(Pv)_j. \tag{38}$$

Choosing each coordinate's upper or lower support according to its coefficient sign gives another bound. Intersecting with the existing interval preserves validity. The reported completion procedure uses two sweeps.

This operation also composes dual certificates. If $c = \sum_j a_j c_j$ with $a_j \geq 0$, let $\lambda = \sum_j a_j \lambda_j$ and $\alpha = \sum_j a_j \alpha_j$. Then $\lambda \geq 0$ and the exact residual is the corresponding linear combination. The triangle inequality makes the resulting support no larger than the same nonnegative combination of previous certified bounds. Applying Equation (38) by selecting objectives $P_{j,:}$ or $-P_{j,:}$ keeps all coefficients nonnegative. The checker can therefore verify completed supports in the original certificate format.

An any-center Mirror lower bound. To obtain a lower bound L on the Mirror cell's enclosing radius, optimize all positive and negative coordinate directions on its normalized section, with barrier levels 10^{-2} through 10^{-7}. Mix each proposed section point with the strict center at weights 0.999 and 0.001. Only exactly Mirror-feasible witnesses are admitted. Exact integer Gram comparisons identify the most separated witness pair. A separate rational cosine check certifies a downward-rounded angle for this pair. Set L to half this certified angle. The triangle inequality makes it a lower bound on the enclosing radius about *any* center. If a checked upper-cap radius U for Full satisfies $U < L$, the same paid ranking therefore certifies an information separation. This computation uses no new endpoint evaluations and does not depend on the pointwise error of a selected estimate.

F.3 Joint analytic centers and their sections

For strict spanning designs, the numerical fit uses a bounded-section analytic center (Goffin & Vial, 2002). Let B encode m row-normalized homogeneous inequalities. Mirror and Reverse use variables $y = v$; Full uses $y = (v, z)$ with one offset fixed. For strictly positive weights w, set $\ell = B^\top w$ and solve

$$\widehat{y} = \operatorname*{arg\,min}_{\ell^\top y = 1,\ By > 0} \left[-\sum_{j=1}^{m} \log(By)_j \right], \qquad \widehat{u} = \widehat{y}_g / \left\| \widehat{y}_g \right\|. \tag{39}$$

Here y_g is the gradient component, and $\ell^\top y = 1$ fixes the scale. Full uses $2n - 1$ adjacent-order rows and $d + n - 1$ variables, enforcing cycles without enumerating them. Reverse uses d variables and permits exact transitive reduction of redundant constraints. Returned directions are checked for feasibility, including the existence of shared offsets for Full.

For n unsigned physical vectors, form features $(x_i, \mathbf{e}_i)$ and $(-x_i, \mathbf{e}_i)$, where $\mathbf{e}_i$ is the pair-indicator vector with one gauge coordinate omitted. Adjacent differences in the full order give a matrix D in $d + n - 1$ variables. Let B be its row-normalized version. Every fit retains all rows.

The first fit uses the positive section normal $e = B^\top w / \left\| B^\top w \right\|$, where $w_i = \lambda_i + 0.01/m$, m is the row count, and $\lambda \geq 0$ is the unit-ball margin solver's dual proposal. Its purpose is to choose a section and a strictly feasible point. If the initial point is not strictly feasible, invertible right whitening or a strict phase-I solve supplies another proposal. The original rows determine acceptance. For the final fit in $d > 3$, use the canonical choice $e = B^\top \mathbf{1} / \left\| B^\top \mathbf{1} \right\|$ and strict phase I. The $d = 3$ fit uses the first section before the geometric selection below.

Both sections are bounded when the physical query matrix spans $\mathbb{R}^d$. Indeed, $By = 0$ makes all endpoint scores equal. Subtracting each mirror pair gives $Xy_g = 0$, hence $y_g = 0$. The fixed gauge then forces all potentials to zero. Thus B is injective. For any strictly positive w, the section $w^\top By = 1$, $By \geq 0$ bounds each slack by $1/w_i$, and injectivity bounds y. The log barrier has a unique minimizer in a nonempty strict section.

The center minimizes $-\sum_i \log(B_i^\top y)$ subject to $e^\top y = 1$. With an orthonormal section basis Q, QR factorization of $\operatorname{diag}(By)^{-1} BQ$ computes Newton steps without forming normal equations. Line search preserves every strict inequality. There are at most 150 iterations, an internal decrement target of 10^{-7}, and a final acceptance threshold of 10^{-5}. The gradient direction must additionally admit an exact shared-potential witness.

The barrier's local metric is not a set certificate. Repeating every row m times leaves the feasible set and analytic center unchanged but multiplies the barrier Hessian by m. Its inverse shrinks by $1/m$ without reducing the direction set. Moreover, different row or section representations can change the selected center. Direction MSE comparisons therefore complement, rather than replace, the representation-independent inclusion witnesses and residual-checked caps.

F.4 Feasible enclosing centers in three dimensions

The spanning Mirror cone is pointed. We enumerate the rays obtained by intersections of pairs of boundary planes of the Reverse outer cone and retain only rays satisfying every row, using exact integer or rational arithmetic. Their nonnegative hull is the entire outer cone. For a proposed center h whose inner products with all rays r_j are positive, define

$$q(h) = \max_j \frac{\|h\|^2 \|r_j\|^2 - (h^\top r_j)^2}{(h^\top r_j)^2}. \tag{40}$$

For every nonnegative ray combination, its tangent norm is at most $\sqrt{q(h)}$ times its parallel component, by the triangle inequality. An outward upper bound on $\sqrt{q(h)}$ therefore encloses the full direction set, since $\arctan(t) \le t$ for $t \ge 0$.

The normalized rays, sums of ray pairs, and both normals through triples give candidate spherical enclosing centers. Choose a proposal that maximizes the minimum dot product with the rays. Mix this proposal with the analytic-center direction using weights $0.9999, 0.99, 0.9, 0.5$. Normalize each mixture and solve the resulting strict difference constraints for the pair potentials. The margin proposals are $2^{-30} \min_i \|x_i\|$ and $2^{-40} \min_i \|x_i\|$. Only candidates satisfying every original ranking edge in exact arithmetic are admitted. The analytic center is also retained. Among these feasible candidates, choose the smallest verified ray cap with a deterministic tie rule. This defines a finite, observation-based selector.

Membership is checked for the returned normalized direction itself. An exact positive rational rescaling of the fitted potentials provides its witness, and every original adjacent edge is rechecked. These checks establish feasibility and cap coverage for the direction actually returned by the implementation.

F.5 A computable chart that contains the robust Full model

The unit-sphere constraint in $\mathcal{C}_\rho$ prevents directly reusing the exact-even homogeneous-cone implementation. We use a certified chart and retain the shared errors explicitly. The construction below takes coordinates, ranks, and error budgets. No target gradient or cardinal score enters it.

F.5.1 Observable axis bound and a checked initialization criterion

Express coordinates and physical error budgets in units of the first public probe radius. Pay for the standard-axis pairs $\pm e_j$ in these units in the first batch. Let $s_j \in \{-1, 1\}$ be an observed mirror sign and $\omega_j \ge 0$ its normalized physical error allowance. For every feasible unit direction v, sign disagreement implies $|v_j| \le \omega_j$. The simpler sufficient bound

$$\ell^\top v \ge \|v\|_1 - 2\sum_j \omega_j \ge 1 - 2\sum_j \omega_j, \qquad \ell = (s_1, \dots, s_d),$$

remains valid. For $S_2 := \sum_j \omega_j^2 < 1$, the observable-initialization experiments use the stronger bound

$$\ell^\top v \ge m_{\mathrm{ax}} := \sqrt{1 - S_2} - S_1, \qquad S_1 := \sum_j \omega_j. \tag{41}$$

To establish it, let J_- be the coordinates with $s_j v_j < 0$. Their squared norm is at most S_2, whereas the matching coordinates have Euclidean norm at least $\sqrt{1 - S_2}$ and hence at least that much ℓ_1 norm. The sum of the disagreeing absolute coordinates is at most S_1. Subtraction gives Equation (41).

When $m_{\mathrm{ax}} > 0$, set $m = m_{\mathrm{ax}}$ or use any positive outward-safe lower bound $m \le m_{\mathrm{ax}}$. Every original feasible direction then has a representative on $\ell^\top w = 1$ with $\|w\|_\infty \le 1/m$. Mirror and reverse-order allowances on this section are ω_i/m and $(\omega_i + \omega_j)/m$. Intersect the implied rows with the coordinate box and apply residual-checked supports. A resulting enclosure with $h^\top v \ge c > 0$ can define the next chart.

Each numerical refinement must preserve *every* direction of the original shared-error model. A support-based norm or cosine tightening is accepted only after its residual-compensated bound is checked. These refinements consume no additional endpoint evaluations. A usable chart is accepted only if its checked error-envelope inflation is at most two. Otherwise the implementation reports that

no usable chart was certified. Keep the section normal ℓ fixed and initialize the outward norm bound $M = 1/m$. Build its Mirror/Reverse polytope with physical allowances $M\omega_i$ and coordinate box $[-M, M]^d$. Compute an interior analytic-center proposal and certify its enclosure. Accept a center h as soon as its checked cosine numerator $c > 0$ satisfies $\|h\|^2 \le 4c^2$. Otherwise tighten M using the support box as follows. Write $z = P_{h^\perp} w$, let $[l_j, u_j]$ enclose each z_j, and let $[L_z, U_z]$ enclose $(P_{h^\perp}\ell)^\top z$. For $\ell^\top h \neq 0$,

$$\|w\|^2 \le \sum_j \max\{l_j^2, u_j^2\} + \frac{\|h\|^2}{(\ell^\top h)^2} \max\{(1 - L_z)^2, (1 - U_z)^2\}.$$

This follows from $w = z + h(1 - \ell^\top z)/(\ell^\top h)$. Round the square root upward, verifying its square against the rational bound, and update only when it strictly reduces M. Recompute the interior point after an update. The first phase allows six such updates with the analytic center as enclosure proposal. A second phase allows three with proposal ℓ. If a phase cannot tighten further, it ends. Every acceptance and update is checked against the enclosing polytope, so unsuccessful numerical proposals cannot remove original feasible directions.

The stronger bound is positive when $S_1^2 + S_2 < 1$. Equal allowances $\omega_j = \rho$ therefore require $\rho < 1/\sqrt{d(d+1)}$, improving the simpler $\rho < 1/(2d)$ test but still having order $1/d$. It is not implied uniformly by every allowed $\rho = O(\varepsilon/\sqrt{d})$ in the information-theoretic localization result. The separate error-contract cohorts use their reported chart checks, rather than this refinement rule.

F.5.2 Shared-error chart, retention, and support verification

On $h^\top w = 1$, fit the entire ranking with

$$\|w\|_\infty \le 1/c, \qquad |b_i| \le \omega_i/c, \qquad \text{scores } e_i \pm (w^\top x_i + b_i), \tag{42}$$

and free shared even potentials. If h is unit, the normalized directions of this fitted set satisfy the sandwich

$$\mathcal{C}_\omega \;\subseteq\; \mathcal{C}_{\text{chart}} \;\subseteq\; \mathcal{C}_{\omega/c}. \tag{43}$$

For the first inclusion, divide any unit candidate and its latent scores by $h^\top v \ge c$. For the second, $h^\top w = 1$ gives $\|w\| \ge 1$. Normalizing a chart candidate can only reduce each error magnitude. With a nonunit stored h, replace the last envelope by $\omega \|h\| /c$. Thus a certified cap with $c/\|h\| \ge 1/2$ costs at most a constant factor in the robust localization theorem. Adding $2d$ paid axis endpoints preserves this endpoint-complexity rate.

To obtain a bounded optimization problem, fix $e_1 = 0$ and choose a potential box without restricting projected directions. For fixed w, b, the ranking constraints are difference constraints in e. If $\|w\|_\infty \le M$, $|b_i| \le B$, and $X_1 = \max_i \|x_i\|_1$, each edge weight has magnitude at most $2(MX_1+B)$. When the system is feasible, shortest-path potentials from a zero-weight supersource have range at most $2n(MX_1 + B)$. Shifting by e_1 therefore permits the box $|e_i| \le 2n(MX_1 + B) + 1$. This removes unbounded potential translations while preserving the candidate directions.

An analytic-center proposal uses all adjacent ranking constraints, the pair-error bounds, and these boxes on the chosen section. QR Newton steps avoid normal equations. A returned coefficient vector must pass exact checks of every ranking inequality and shared-error bound. The same initial chart is reused across later shells, retaining each endpoint's physical budget and every earlier constraint. These fitted models are nested and always contain the true direction when the contracts hold.

For certification, eliminate the even potentials using Mirror and reverse-order relations, now with their bounded-error allowances. On a section $\ell^\top w = 1$, let $Gw \le b$ be this gradient outer polytope and $\|w\|_\infty \le M$. Any $\lambda \ge 0$ gives the exactly checkable support bound

$$q^\top w \le \lambda^\top b + \alpha + M \left\| q - G^\top \lambda - \alpha\ell \right\|_1. \tag{44}$$

Tangent-coordinate bounds and a positive parallel bound yield a cap as in Appendix F. If its squared tangent ratio is Q about stored center h, then any positive rational c with $c^2(1 + Q) \le \|h\|^2$ is a valid lower bound on $h^\top v$ for unit candidates. All support products, residual allowances, and this last inequality are recomputed in rational arithmetic. Loose bounds affect informativeness, not validity.

G INFORMATION GEOMETRY: SCALE, NUISANCE RANK, AND CYCLES

These experiments measure information under matched endpoints. Scale and nuisance-family controls assess when cross-pair orders are useful. Exact cycle witnesses distinguish Full from Reverse. The cubic branches test model validity and are reported in Appendix J.

G.1 STRUCTURAL EXPERIMENTS: PROTOCOL

G.1.1 TARGETS, PAIRED DESIGNS, AND ENDPOINT ACCOUNTING

The structural study has 96 independent target–axis units, 32 at each $d \in \{3, 8, 20\}$, separate from Appendix G.4. Normalize independent Gaussian vectors to obtain u, z, and normalize $z - (z^\top u)u$ to obtain q. Generate $16d$ uniform unsigned directions from normalized Gaussian draws. Budget N uses the first $N/2$ directions and their antipodes, sharing targets, axes, and prefixes across coefficients and families. Exact seed formulas for all studies are in the companion `seed_manifest.csv`.

The experiment matrix is:

- Quadratic: $N/d \in \{4, 8, 16, 32\}$ and $\lambda \in \{0, 10^{-3}, 10^{-2}, 10^{-1}, 1, 10^2, 10^4\}$, giving 2,688 conditions.
- Quartic even: $N/d \in \{8, 32\}$ and $\lambda \in \{10^{-3}, 10^{-1}, 1\}$, giving 576 conditions.

These 3,264 even-family conditions reuse 96 independent units; MSEs average all 32 targets per dimension. The odd-remainder branch uses the same units and is specified with its retention policies and diagnostics in Appendix J.1.

G.1.2 FUNCTION FAMILIES AND PHYSICAL SHELLS

For positive λ, the quadratic family is

$$f_\lambda(x) = u^\top x + \tfrac{1}{2} t \|x\|^2 + \lambda (z^\top x)^2, \qquad t = 100\lambda. \tag{45}$$

For unit u, z, $H = t(I + 0.02 z z^\top)$ has condition number 1.02 and $\tau_1 = \lambda$. At $\lambda = 0$, $t = 1$ gives the isotropic baseline. The quartic family uses

$$f_\lambda(x) = u^\top x + \tfrac{1}{2} \|x\|^2 + \lambda (z^\top x)^4. \tag{46}$$

Its nominal unit-shell variation is also λ, with no quadratic representation of the last term. Both families use one uniform antipodal batch at physical radius one. The joint decoder is given no coefficient, curvature, or nuisance-family information.

All coordinates and polynomial coefficients are stored in float64. Exact checks treat these stored values as binary rationals. Consequently nominal unit norms and orthogonality need not hold as real-arithmetic identities at the saved points. The evaluator uses their actual norms and coordinates.

G.1.3 RECOVERY AND NUMERICAL VERIFICATION

The Full solver and selector are specified in Appendix F. Python 3.12 and CUDA float64 produce numerical proposals. Exact CPU arithmetic checks their feasibility and bound residuals. A float64 score enclosure detects ambiguous polynomial orders, which are resolved at exact stored-coordinate values. The decoder receives only coordinates and integer ranks.

For each proposed or true direction, exact difference constraints produce shared potentials or a negative-cycle witness, testing membership in the Full projection rather than its Reverse outer cone. Independent checks verify returned-direction feasibility, outer caps, and Mirror lower-bound witnesses (Appendices F and F.2). All planned branches are checked, and completed even fits meet the analytic-center residual requirement. Projection and replay checks use stored observations, adding neither endpoints nor independent targets.

G.1.4 EXACT COMPARISONS OF THREE DIRECTION SETS

The projection audit uses all 32 three-dimensional targets at $N/d = 8, 32$ and $\lambda = 0, 10^{-3}, 10^{-1}, 1, 10^4$, for 320 conditions. It starts from the exact Mirror and Reverse cones. Each extreme ray of the

Table 4: One-round Full MSE for quadratic nuisance (rad^2). Each entry averages 32 independent targets per dimension. Targets and query prefixes are shared across budgets and shell-variation levels.

d	λ	$N/d = 4$	8	16	32
3	0	1.669×10^{-2}	1.044×10^{-3}	4.299×10^{-5}	3.877×10^{-6}
3	10^{-3}	1.669×10^{-2}	1.044×10^{-3}	4.291×10^{-5}	4.040×10^{-6}
3	10^{-2}	1.694×10^{-2}	9.970×10^{-4}	3.978×10^{-5}	6.087×10^{-6}
3	10^{-1}	1.999×10^{-2}	1.307×10^{-3}	1.867×10^{-4}	3.647×10^{-5}
3	1	4.119×10^{-2}	5.796×10^{-3}	1.344×10^{-3}	2.233×10^{-4}
3	10^2	2.039×10^{-1}	4.622×10^{-2}	1.895×10^{-2}	3.042×10^{-3}
3	10^4	2.202×10^{-1}	7.419×10^{-2}	2.836×10^{-2}	5.807×10^{-3}
8	0	5.496×10^{-3}	1.502×10^{-4}	8.985×10^{-6}	5.078×10^{-7}
8	10^{-3}	5.452×10^{-3}	1.506×10^{-4}	9.195×10^{-6}	5.091×10^{-7}
8	10^{-2}	5.651×10^{-3}	1.457×10^{-4}	1.323×10^{-5}	9.758×10^{-7}
8	10^{-1}	4.805×10^{-3}	1.995×10^{-4}	2.082×10^{-5}	2.246×10^{-6}
8	1	1.060×10^{-2}	3.325×10^{-4}	3.472×10^{-5}	3.840×10^{-6}
8	10^2	2.112×10^{-1}	2.134×10^{-2}	4.510×10^{-3}	4.854×10^{-4}
8	10^4	3.552×10^{-1}	7.441×10^{-2}	2.484×10^{-2}	7.232×10^{-3}
20	0	9.471×10^{-4}	3.739×10^{-5}	1.525×10^{-6}	1.007×10^{-7}
20	10^{-3}	9.405×10^{-4}	3.813×10^{-5}	1.600×10^{-6}	1.179×10^{-7}
20	10^{-2}	8.800×10^{-4}	3.299×10^{-5}	2.087×10^{-6}	1.968×10^{-7}
20	10^{-1}	7.888×10^{-4}	4.340×10^{-5}	3.904×10^{-6}	3.534×10^{-7}
20	1	1.267×10^{-3}	6.208×10^{-5}	5.090×10^{-6}	4.788×10^{-7}
20	10^2	9.628×10^{-2}	6.874×10^{-3}	4.720×10^{-4}	4.504×10^{-5}
20	10^4	3.431×10^{-1}	7.938×10^{-2}	2.423×10^{-2}	5.577×10^{-3}

Reverse cone is tested against all ranking difference constraints. An infeasible ray supplies a negative cycle and hence a valid gradient halfspace. Add that halfspace, recompute the exact extreme rays, and continue until every ray admits shared potentials.

At termination, the resulting cone equals the Full gradient projection. Every cut is implied by the ranking, so the Full projection is contained in the computed cone. Conversely, feasibility of all generating rays puts their nonnegative hull inside the convex projected cone. A removed Reverse ray establishes a strict inclusion. Equality with the Mirror cone is checked by exact canonical extreme rays. These operations use the saved endpoints and require no new evaluations.

For each cone, the most separated ray pair supplies an any-center angular-radius lower bound. A common strictly feasible unit center supplies a tangent-ratio upper bound. If every ray v has $h^\top v > 0$, then

$$\operatorname{angle}(h, v) = \arctan\left(\frac{\left\|v - (h^\top v)h\right\|}{h^\top v}\right) \le \frac{\left\|v - (h^\top v)h\right\|}{h^\top v}.$$

Exact Gram comparisons and outward rounding certify the maximum ratio. It also bounds the cone's normalized convex combinations. The reported Full/Reverse cap ratio uses this same center. It is not the ratio of optimal enclosing radii.

G.2 Structural experiments: supporting results

G.2.1 Scale dependence and finite-budget recovery

Table 4 reports absolute direction MSEs, complementary to the information ratios in Figure 2. Larger budgets reduce MSE at every tested scale, but large-scale errors remain higher despite condition number 1.02. All 2,688 quadratic conditions preserve true-direction feasibility and cap coverage. Losing ranking gain is not model invalidity or loss of all mirror information.

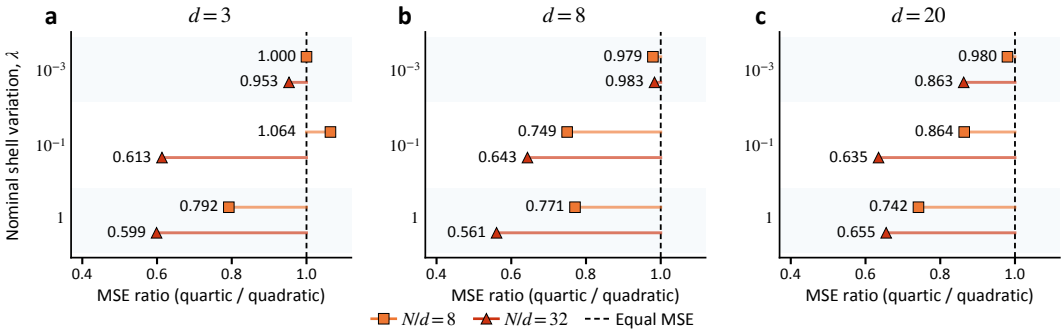

Figure 6: Recovery under quartic and quadratic even nuisance. Labels show quartic/quadratic MSE ratios over 32 matched targets at matched nominal shell variation. Shell-variation levels are tested categories, not a continuous logarithmic axis. Segments connect estimates to equality; they are not confidence intervals.

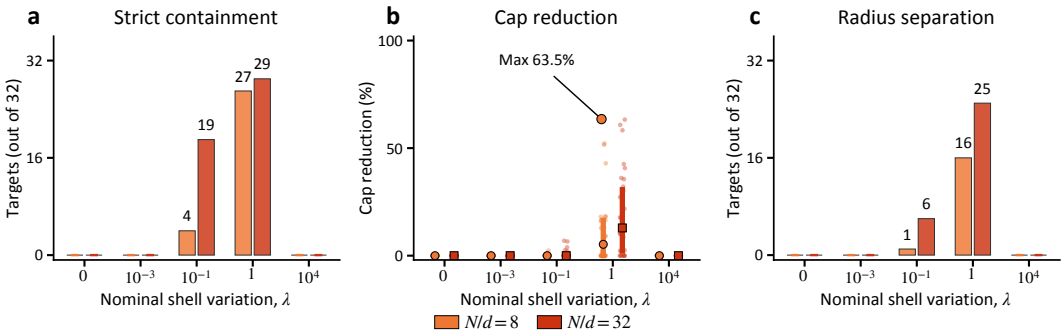

Figure 7: Exact three-dimensional projected-cone geometry. Each shell-variation level and budget uses 32 targets. (a) Counts show strict inclusion of Full in Reverse. (b) $100(1 - U_F/U_R)$ gives the percentage reduction in upper cap radii about a common center. Small points show targets, large marks medians, and bars interquartile ranges. (c) Counts show $U_F < L_R$, where L_R is the Reverse any-center lower bound. Shell-variation levels are tested categories. All 320 conditions use matched endpoints.

G.2.2 Nonquadratic even nuisance

Figure 6 compares all 18 matched dimension–budget–variation configurations. At $\lambda = 1$, quartic MSE is lower in every configuration. Shell variation gives a worst-case guarantee but does not uniquely determine realized information. All 576 quartic conditions preserve true-direction feasibility, cap coverage, and $U < L$ without fitting either nuisance family. Absolute quartic MSEs are retained in the companion `table04_quartic_mse.csv`.

G.2.3 The additional information in longer cycles

The 79 strict inclusions and 48 radius separations in Figure 7 are distinct diagnostics. Available bounds need not detect every smaller cell. At the largest scale, all 64 checked Full cones equal their Mirror cones. These are finite-design observations; Theorem 3 supplies the minimax conclusion.

G.3 Matched rank-one and higher-rank anisotropy

Figure 3 reports the main model-layer and cycle-witness results. This section gives their design, resampling, and computational scope.

G.3.1 Design and the controlled difficulty change

The matched-rank study uses Equation (13) with twelve independent target–reflection–design units, four at each $d = 8, 20, 50$. The settings are $N/d \in \{8, 16\}$, $\lambda \in \{10^{-3}, 10^{-1}, 1\}$, and $k \in \{1, d/2\}$. Target and query directions are independent isotropic draws. The 144 family conditions give 432 Mirror/Reverse/Full outputs. All three models use the same endpoints within a condition. The reflection is $Q = I - 2zz^\top/(z^\top z)$ for a stored nonzero integer vector z, with rational entries. Gaussian targets and query vectors are normalized in float64. Exact ordering and support checks use those stored coordinates. The seed manifest and source snapshots fix target, reflection, and query-prefix generation. Companion files `high_rank_all_outputs.csv` and `high_rank_all_groups.csv` contain all 432 model outputs and 108 model–dimension–budget–scale summaries, respectively, under `data/integrated_20260918/`.

A separate confirmation retains the frozen query, fit, and certificate rules. It uses twelve additional units, with four per dimension, at $N = 8d$ and $\lambda = 0.1$ (base seed 8818091901). All 72 model runs complete. All 24 rank-family conditions certify separation between Full and Mirror. Each also admits a Reverse-feasible direction that Full excludes through a negative cycle. For the high-rank family, the confirmation-only pooled Full/Mirror and Full/Reverse MSE ratios are 0.0009903 and 0.4784. These ratios use a different aggregation scheme from the primary figure. The cohort is reported separately in `confirmation_high_rank_outputs.csv`.

The comparison matches the minimum and maximum eigenvalues and the condition number while changing the rank of the anisotropic part. The ideal uniform-sphere moments in Appendix B.1 explain the resulting change in difficulty. For unit W uniform on the sphere and any fixed orthogonal Q,

$$\mathrm{Var}\Big(\big\|P_k Q^\top W\big\|^2\Big) = \frac{2k(d-k)}{d^2(d+2)}, \qquad \mathrm{Var}(g^\top W) = \frac{\|g\|^2}{d}.$$

Consequently the standard-deviation ratio of the anisotropic nuisance to the linear signal is

$$\frac{\lambda}{\|g\|}\sqrt{\frac{2k(d-k)}{d(d+2)}}.$$

For $k = 1$ this decreases as $d^{-1/2}$. For $k = d/2$ it stays of constant order at fixed $\lambda/\|g\|$. These ideal-sphere moments describe typical, rather than worst-case, variation and require no Haar assumption on Q.

G.3.2 Point loss, set witnesses, and computation

Under high-rank nuisance, Full's pooled MSE is 1.447 times its value under rank-one nuisance (marginal paired 95% interval $[1.175, 2.127]$). This contrast is exploratory. Unlike exact cycle witnesses, MSE also depends on the analytic-center selector.

The marginal interval above uses 10,000 dimension-stratified target resamples, preserving both budgets, all three scales, and both ranks within an independent unit. With four independent units per dimension, repeated conditions increase within-unit coverage of settings but do not create additional independent targets.

In Figure 3(a), Full/Mirror MSE ratios pool both budgets and all three scales *within each unit and rank*. In panel (b), Full/Reverse ratios pool both budgets within each unit, rank, and fixed scale. If A_j and B_j are these paired mean squared angular errors for the numerator and denominator models, the pooled statistic is $\sum_j A_j / \sum_j B_j$. Within-unit ratios A_j/B_j are paired diagnostics; their arithmetic mean generally differs from the pooled statistic. Panel (a) has four such units per dimension and panel (b) twelve per scale. Intervals concern pooled estimates, not individual settings. Shell-variation levels in Figure 3 are tested categories. Panel (b)'s small-point shapes indicate dimension, and connecting lines are not confidence bands.

At $\lambda = 10^{-3}$, the exact negative-cycle witness counts are 1/24 for rank-one nuisance and 7/24 for high-rank nuisance. At each of $\lambda = 10^{-1}, 1$, both families have 24/24. A witness provides a direction allowed by Reverse but ruled out by a longer ranking cycle. Failure to find one does not establish equality. Unlike the three-dimensional exhaustive projection audit, this experiment does not enumerate the complete high-dimensional projected cone or its optimal enclosing radius.

The Full and Reverse selectors use different analytic-center barriers (Appendix F), and the high-dimensional Full upper cap encloses Reverse. At $d = 50$, median Full/Reverse fitting times are $0.323/0.080$ seconds, whereas both certificate times are approximately 17.68 seconds. Hardware and instance differences preclude a direct timing comparison with Appendix K.

G.4 Additional independent first-batch information audit

This audit uses the saved first batches of a separate two-round cohort. Its objective is

$$f(x) = u^\top x + \tfrac{1}{2}\|x\|^2 + \lambda(z^\top x)^2, \qquad \|u\| = \|z\| = 1. \tag{47}$$

Independent normalized Gaussians give a fixed target–axis pair (u, z). There are 256 independent units at each $d \in \{3, 8, 20\}$, separate from the structural cohort. Each is reused across the original total-budget labels $B/d \in \{16, 32\}$ and $\lambda \in \{0.001, 0.1\}$, giving 768 units and 3,072 first-batch conditions. A saved first batch consists of $B/2 \in \{8d, 16d\}$ endpoints: $B/4$ independent uniform unsigned directions and their antipodes at radius one. Only this first batch contributes to the reported observations and endpoint costs. The companion seed manifest specifies the fixed designs.

Stored float64 normalizations need not satisfy ideal unit norms exactly. For the polynomial defined by stored u, z, the ideal radius-a relative shell variation is $a\lambda\|z\|^2 / \|u\|$. Actual stored-coordinate evaluation also includes the isotropic term. Float64 polynomial scores use a 10^{-12} coarse enclosure, with ambiguous adjacent orders resolved by exact binary-rational values. The decoder receives only coordinates and ranks. The numerical fit and independent feasibility/support checks use Appendix F.

The saved first-batch upper bound U encloses the Reverse cone and hence Full. In $d > 3$ its center is the first-section joint analytic-center direction. In $d = 3$, the saved center is the feasible midpoint between the analytic-center and enclosing-center directions. Rescale the two joint coefficient vectors to unit gradient parts, average them with equal weight, and normalize the resulting gradient part. Positive combinations preserve strict homogeneous ranking inequalities. The actual rounded coefficient vector and its ray cap are checked again. This retains the original certificate center rather than recomputing the reported bounds with a different selector. The any-center Mirror lower bound L is constructed by Appendix F.2. Both bounds use the same first-batch endpoints, with no new oracle evaluations.

The audit certifies $U < L$ in all 1,536 conditions at $\lambda = 0.001$ and in 1,533 of 1,536 at $\lambda = 0.1$. The three unresolved comparisons are all at $d = 20, B = 16d, \lambda = 0.1$, with maximum $U/L = 6.061$. Nonseparation does not establish cone equality. All first-batch caps cover the true direction. Median U/L decreases with budget and increases with nuisance coefficient in every dimension. These geometric results are descriptive. Complete grouped summaries are identified by `table09_information.csv`.

H Ranking-Only Optimization on Real-Data Quadratic Tasks

H.1 Tasks, information access, and the local model

The tasks are UCI Airfoil Self-Noise and Concrete Compressive Strength (Brooks et al., 1989; Yeh, 1998). Each uses a fixed 80/20 split and training-only standardization. Hessian whitening is not applied. Including the unpenalized intercept gives $d = 6$ and $d = 9$. The reported objective is half the mean squared training residual plus a ridge penalty of weight 0.01 on feature coefficients. Writing R_{quad} for the quadratic regularizer, the objective is

$$F(\theta) = \frac{1}{2m}\|X\theta - y\|^2 + R_{\mathrm{quad}}(\theta), \qquad R_{\mathrm{quad}}(\theta) = \frac{0.01}{2}\|\theta_{1,\dots,d-1}\|^2.$$

For any center θ_c its exact expansion is

$$F(\theta_c + x) = F(\theta_c) + \nabla F(\theta_c)^\top x + \tfrac{1}{2}x^\top H x.$$

Thus recovery is within the even model at every center, with the data covariance unchanged. For dataset identifier j, NumPy's default generator with seed $202609170 + j$ permutes the rows. The first $\lfloor 0.8 m_{\mathrm{total}} \rfloor$ are training data. Feature and response means and population standard deviations are estimated on training rows only. The standardized response is $(y - \overline{y}_{\mathrm{train}})/s_{y,\mathrm{train}}$. Test RMSE is

converted back to the original response scale by multiplying by $s_{y,\mathrm{train}}$. The initial feature coefficients are zero and the unpenalized intercept is one. Exact split indices and stored scaling constants are supplied in `dataset_split_indices.csv` and `training_scalings.csv`.

Only endpoint coordinates and rankings enter the online query and step decisions. The exact optimum and held-out test scores are reserved for evaluation. Hyperparameters are selected using terminal training objectives on separate development seeds. At every new optimization center, the gradient consistency model is rebuilt from scratch.

The primary optimization metric is

$$r(\theta) = \frac{F(\theta) - F^\star}{F(\theta_0) - F^\star}.$$

It measures the fraction of the initial optimization gap remaining. The 32-seed intervals hold the train/test split fixed and quantify algorithmic randomness. They do not establish uncertainty over alternate data splits or a task population.

H.2 Information-layer trajectories

Mirror, Reverse, and Full receive $8d$ recovery endpoints at every center and thirteen paid dyadic step candidates, including the current center. Eight updates therefore spend $8(8d + 13) = 488/680$ endpoints on Airfoil/Concrete, with sixteen feedback rounds. The study uses radii $1/8, 1/64$ and 32 algorithm seeds per task, paired across all methods and radii, giving $2 \times 2 \times 32 \times 3 = 384$ completed trajectories.

Panel A of Table 2 reports all four task–radius comparisons. Intervals use 20,000 paired algorithm-seed resamples. Bonferroni adjustment covers eight contrasts. Ratios compare arithmetic means of relative gaps; they are not means of per-seed ratios. Concrete test RMSE is 11.0048 for Mirror and approximately 10.9618 for Full. At each center, all three recovery models return unit directions. The step grid is $\{0, 2^{-10}, 2^{-9}, \ldots, 2^{1}\}$. It is applied directly to those directions without gradient-magnitude scaling. `ridge_model_absolute_results.csv` gives all twelve task–radius–method rows, including absolute mean relative gaps and test RMSEs. `ridge_model_contrasts.csv` gives the eight paired gap contrasts and paired test-RMSE differences. All per-iteration outcomes are retained in `ridge_all_trajectories.csv`.

H.3 External optimizer implementations and development

The controls are ZO-RankSGD (Tang et al., 2024), STP (Bergou et al., 2020), CMA-ES (Hansen & Ostermeier, 2001), and local incumbent random search. Each method uses its own queries and returns the best paid point. ZO-RankSGD uses Gaussian ranking estimates and an ordinal line search. STP uses fixed or decreasing steps. CMA-ES uses native EvoTorch 0.6.1 GPU execution with rank fitness and its default active covariance adaptation.

For each task and resource profile, twelve configurations per method are evaluated on four development seeds. CMA-ES additionally includes four configurations with population size $\lfloor (B-1)/16 \rfloor$, enabling effective use of the round cap. Selection minimizes the terminal development training objective without test-based tuning. Final evaluation uses 32 algorithm seeds, five methods, two tasks, and two resource profiles, giving 640 completed trajectories. With $m = 8d$ Gaussian samples z_i and ranks $r_i \in \{0, \ldots, m-1\}$ increasing with loss, ZO-RankSGD uses $\sum_i (2r_i - m + 1) z_i / \binom{m}{2}$. This estimator is not normalized before line search. Full uses a unit direction. Both evaluate $\{0, b2^{-11}, \ldots, b\}$ times their direction, where b is the selected step parameter. CMA-ES minimizes within-batch ranks. Its covariance update receives no cardinal losses. The configuration grids and selected task–resource settings are stored in `external_development_plan.json`, `external_cma_budget_grid.json` and `external_selected_configurations.json`. Development and evaluation use disjoint base seeds 1709186201 and 1709187201, respectively, with the dataset and replicate offsets recorded in the manifests.

The Reverse attribution control repeats the Full grid and development budget, but replaces the Full joint fit by the Mirror and reverse-order rows defining $\mathcal{C}_{\mathrm{rev}}$. Exact transitive reduction removes only rows implied by retained paths. The resulting fit uses an analytic-center direction selector and the same unit-direction line search. All 192 development trajectories complete. The deterministic

Table 5: Realized resources for external comparisons. Entries give Airfoil/Concrete endpoint and feedback-round counts under joint endpoint–round caps or an endpoint cap alone. Common caps need not be fully spent by every method.

	Joint caps		Endpoint cap only	
Method	Endpoints	Rounds	Endpoints	Rounds
Full	489 / 681	16 / 16	489 / 681	16 / 16
Reverse	489 / 681	16 / 16	489 / 681	16 / 16
ZO-RankSGD	489 / 681	16 / 16	489 / 681	16 / 16
STP	33 / 33	16 / 16	489 / 681	244 / 340
CMA-ES	481 / 673	16 / 16	487 / 681	54 / 68
Random	481 / 673	16 / 16	489 / 681	17 / 17

selection rule chooses query radius $1/64$ on Airfoil and $1/16$ on Concrete, with unit step scale, for both resource profiles. These are also the configurations selected independently for Full. The Reverse development optimum is tied across the two tested step maxima in each task. The fixed configuration-index rule selects the smaller maximum.

Confirmation uses the same 32 algorithm seeds per task and resource profile, giving 128 additional complete trajectories. Full and Reverse have identical initial centers, random direction arrays, paid first batches, and observed first-batch scores. Their later centers and queries may diverge. The targeted study defines two diagnostic families before confirmation analysis: four Full/Reverse contrasts across terminal relative gap and test RMSE, and sixteen Reverse/control terminal-gap contrasts across both resource profiles. No result is pooled with the earlier information-layer trajectories.

Attribution and reporting limits. These comparisons do not isolate the estimator's contribution. ZO-RankSGD is not unit-normalized before line search, and the ridge study lacks a unit-normalized control or a Mirror external-control arm. Random-search proposal distributions and step scales are not specified here. The complete tuning grids are confined to companion records, limiting assessment of search-space fairness. The unit-normalized control in Appendix I.4 belongs to a different task cohort and does not resolve this ridge-specific limitation.

H.4 Endpoint and feedback-round accounting

For Full and Reverse, the external comparison charges a separate initial incumbent evaluation in addition to eight recovery/step updates, giving $B = 1 + 8(8d + 13) = 489/681$, one endpoint more than the information-layer trajectories (Table 5).

The initial incumbent is appended to the first submitted batch before any scores are returned. That call charges all its endpoints and increments the round counter once. Each subsequent call similarly submits its entire batch before feedback. Reconstructing the original 30,848 stored batches across 640 runs confirms the endpoint totals, round totals, and first-batch incumbent in every run. The Reverse control adds 2,048 independently recomputed batches. This gives 32,896 audited batches in total. All 128 Reverse outputs are the best paid point in their history. All 128 first batches match Full exactly. `external_batch_ledger.csv` records the original batch index, new and cumulative endpoint counts, and preceding feedback dependency. `external_reverse_audit.json` records the targeted audit.

Sequential STP stores the incumbent and spends only two new endpoints per update, so it cannot use the endpoint cap within sixteen rounds. Its poor round-capped result is therefore not evidence of poor sequential FE efficiency. CMA-ES includes round-aware populations, and ZO-RankSGD spends essentially the same FE budget as Full, supplying batch-capable controls.

H.5 Effects and statistical scope

For the Full/control comparison in Figure 4, 40,000 paired algorithm-seed resamples give percentile intervals with Bonferroni adjustment over sixteen contrasts spanning both resource profiles. The eight displayed joint-cap intervals lie below one. Full/ZO-RankSGD terminal mean-gap ratios are $0.358\,[0.168, 0.845]$ on Airfoil and $0.646\,[0.498, 0.837]$ on Concrete. Full/CMA-ES ratios

are $0.0658\,[0.0328, 0.1226]$ and $0.223\,[0.177, 0.289]$, respectively. `external_all_contrasts.csv` reports the numerical results for every contrast in the comparison family.

Panel B of Table 2 reports the independently tuned Full/Reverse and Reverse/control terminal-gap ratios. The Full/Reverse family has four contrasts, spanning two tasks and terminal gap/test RMSE. Its additional test-RMSE ratios are $0.99970\,[0.99925, 1.00011]$ on Airfoil and $1.00000\,[0.99907, 1.00095]$ on Concrete. These intervals use the same 40,000 paired resamples and four-contrast Bonferroni adjustment. None of the four Full/Reverse intervals excludes one. Reverse/control intervals use their separate sixteen-contrast family spanning both resource profiles, not the four-contrast adjustment.

Absolute results and both attribution families are identified by `external_reverse_all_groups.csv`, `external_full_reverse_contrasts.csv`, and `external_reverse_control_contrasts.csv`. Development selections and audit receipts appear in `external_reverse_audit.json`. Under endpoint-only caps, Full and Reverse complete eight updates in sixteen rounds. STP and CMA-ES use additional rounds and attain lower mean gaps (Tables 3 and 5). These endpoint-only comparisons are descriptive.

Mean Airfoil/Concrete runtimes are $0.62/0.82$ seconds for Full, $0.43/0.61$ for Reverse, and $0.10/0.05$ for ZO-RankSGD. Full and ZO-RankSGD test RMSEs are $4.7102/10.9544$ and $4.7190/11.0208$, respectively. Reverse's test RMSEs are $4.7116/10.9544$. Reverse's mean whole-run times are 30% and 26% lower than Full's in these implementations. The runs were executed separately, so this is a descriptive implementation result, not a general timing ratio. This pipeline comparison does not isolate a benefit from computing a certificate at every center.

The external-run timer starts before loading the processed task and constructing GPU tensors, and ends after optimization, diagnostic metrics, and compressed query-record output. It includes direction fitting, rank sorting, query generation, and the algorithm's objective evaluations. It is a whole-run measurement, not a certificate-only or optimizer-kernel timer. No warm-up is subtracted. Objective calls synchronize the GPU before and after evaluation and also have a separately recorded timer. Independent audit programs run afterward and are excluded. Whole-run times and the separately reported component costs in Appendix K therefore have different scopes.

The task interface combines within-batch ranks with an ordinal incumbent update. The evaluator privately compares each new batch's best point with the stored incumbent and exposes the coordinates of the best paid point, but not its score. The saved-batch audit independently verifies that every final output is the best evaluated point across the complete history.

I Non-Even Logistic Recovery and Local-Step Controls

Recovery validity and downstream local-step outcomes use the same task cohort but different paid observation stages. Validity is assessed before step feedback. The subsequent fixed-center comparisons evaluate recovery-and-step procedures, not moving-center optimization or a calibrated-descent guarantee.

I.1 Tasks and nonzero recovery centers

The two classification datasets are UCI Blood Transfusion Service Center and Banknote Authentication (Yeh, 2008; Lohweg, 2012). Fixed 80/20 splits and training-only standardization yield $d = 4, 5$ parameters including the intercept. In Blood, exact affine-duplicate detection using training data removes Monetary, which is 250 times Frequency. Every compared method uses the same resulting features. Feature coefficients start at zero, and the unpenalized intercept starts at 0.5.

For a scalar logit t,

$$\log(1 + e^t) - yt = \log(2\cosh(t/2)) + (1/2 - y)t.$$

At the all-zero parameter, the logistic objective is itself linear-plus-even. The nonzero-center experiment avoids this special expansion. The numerical audit reports a nonzero odd remainder in every tested condition at the prescribed nonzero center.

I.2 PUBLIC SMOOTHNESS, THIRD DERIVATIVE, AND GRADIENT CALIBRATION

Write X_i for augmented training features, m for training size, σ for the logistic sigmoid, and $\overline{y}$ for the training-label mean. The supplied outward-rounded constants are

$$L = \frac{1}{4m}\sum_i \|X_i\|^2 + 0.01, \qquad M_3 = \frac{1}{6\sqrt{3}\,m}\sum_i \|X_i\|^3, \qquad 0 < g_{\min} < |\sigma(0.5) - \overline{y}|.$$

They use task metadata and the prescribed center, not the realized full gradient or ranking margins. The intercept derivative at this center is exactly $\sigma(0.5) - \overline{y}$, so its absolute value is a gradient-norm lower bound. It need not remain a lower bound after moving the center.

For the scalar logistic loss, its second derivative is at most $1/4$, and the absolute third derivative is at most $1/(6\sqrt{3})$. The implemented training objective is

$$F(\theta) = \frac{1}{m}\sum_i \left[\log(1 + e^{X_i^\top \theta}) - y_i X_i^\top \theta\right] + \frac{0.01}{2}\,\|\theta_{1,\ldots,d-1}\|^2.$$

The unpenalized intercept is the last coordinate, so the regularizer contributes exactly 0.01 to the Hessian operator-norm bound. Summing feature-tensor bounds gives the displayed L and M_3. The stored $(L, M_3, g_{\min})$ values are

$$\begin{aligned} \text{Blood:} \quad & (1.0100000000000005, 1.1487774432367968, 0.3850011272219215), \\ \text{Banknote:} \quad & (1.2600000000000013, 1.2690047823460824, 0.16940553815718729). \end{aligned}$$

Interval arithmetic verifies that the first two are rounded outward and that the last is strictly below the absolute intercept derivative.

With physical radius a, stored score error bounded by ν, and numerical allowance 10^{-10}, the fitted shell-normalized shared error is

$$\rho_a^{\text{fit}} = \frac{M_3 a^2/6 + (\nu + 10^{-10})/a}{g_{\min}}. \tag{48}$$

In common physical-score coordinates it is $a\rho_a^{\text{fit}} = [M_3 a^3/6 + \nu + 10^{-10}]/g_{\min}$. The two representations must not be interchanged when retaining several shells. The cubic term controls odd remainder, not even Hessian anisotropy. A valid error contract alone does not verify the fast-localization sufficient condition on τ_a.

For $\nu > 0$, each endpoint receives one stored uniform error in $[-\nu, \nu]$. It keeps that realized error in the ranking. The resulting observations remain transitive. The public constants are expressed on the task's calibrated score scale, so the experiment is not scale-free under an arbitrary unknown monotone score transformation. We verify the numerical contract with 192-bit Arb ball arithmetic, treating the stored float64 features, labels, and regularizer coefficient as exact inputs. The audit encloses dot products, exponentials, logarithms, sums, and the calibration formulas. For recovery, it evaluates the ideal points $\theta_0 \pm aW_i$, thereby including coordinate-construction rounding in the score-error check. All 256 conditions pass. The largest recovery-batch clean-score discrepancy upper bound is $3.88 \times 10^{-16} < 10^{-10}$, and every observed pair satisfies its gradient-normalized shared-error allowance. Detailed receipts are in `logistic_interval_and_centers.csv` and `logistic_interval_summary.json`.

I.3 MATCHED RECOVERY-STAGE VALIDITY

Sixteen query/noise seeds per task are reused across $a \in \{1/4, 1/8, 1/32, 1/128\}$ and $\nu \in \{0, 10^{-5}\}$. The resulting 256 conditions reuse 32 dataset–seed units. For the recovery-stage comparison, zero-error Full, robust Reverse, and robust Full receive identical $8d$ antipodal endpoints, with paid axis initialization included in that first batch. This stage costs one feedback round and $32/40$ endpoints on Blood/Banknote. The local-step arms in Appendix I.4 add a separate paid round. No observations from that additional round enter the recovery-stage validity or cap summaries.

Every robust initialization meets the checked factor-two chart criterion, and every robust fit retains the true direction and every cap covers it. The zero-error Full model excludes the true direction

in thirteen conditions, including three with $\nu = 0$. The fitted cell and its outer cap are checked separately. Coverage alone would not establish that a misspecified model contains the true direction.

Figure 5 shows all radius/noise conditions. In panel (b), solid and dashed lines denote zero and nonzero score-error bounds, respectively. For $\nu = 10^{-5}$, the mean caps on Blood/Banknote are $0.2164/0.6842$ at $a = 1/4$. They are $0.0780/0.0833$ at $a = 1/32$ and $0.0807/0.1089$ at $a = 1/128$. Figure 5(c) compares the two terms in the implemented allowance. The diagonal marks equality. Their score-error/odd-remainder ratio is $6(\nu + 10^{-10})/(M_3 a^3)$; the factor $g_{\min}$ cancels. Ratios below/above one indicate odd-remainder/score-error dominance. A crossing of one is consistent with the observed small-radius upturn, but it does not define a universally optimal radius. All 256 conditions, including every zero-error exclusion, remain in these recovery summaries. The corresponding recovery and local-step records are identified by `logistic_all_outputs.csv` and `logistic_absolute_results.csv`.

I.4 Matched-budget local-step comparisons and physical-step control

What is matched. The four local-step arms are zero-error Full, robust Reverse, robust Full, and ZO-RankSGD. The first three reuse the identical $8d$ antipodal recovery endpoints described above. ZO-RankSGD receives $8d$ Gaussian endpoints with matched root-mean-square radius. Later step candidates can differ with the fitted direction. Comparisons with ZO-RankSGD instead match the budget but use different recovery-query geometry.

Each arm then evaluates thirteen candidates on the fixed dyadic multiplier grid $\{0, 2^{-10}, 2^{-9}, \ldots, 2^{1}\}$ with unit base scale. This adds a second feedback round, giving $8d + 13$ endpoints: 45 on Blood and 53 on Banknote. All 1,024 runs complete, and the zero-error arm's exclusions remain recorded. Zero-error Full and both robust models use unit directions. ZO-RankSGD uses its unnormalized complete-ranking Gaussian estimate. Identical multipliers therefore do not imply identical physical step lengths. No arm uses L or $g_{\min}$ to tune the step grid. The robust models use calibration to construct their feasible sets. The reported interval audit also checks the saved line-search and ZO-RankSGD observations under the numerical contract in Appendix I.2. Those checks do not change the recovery-stage sample count.

Unit-normalized physical-step control. A separate diagnostic normalizes the saved ZO-RankSGD estimate $\widehat{g}$ when $\|\widehat{g}\| > 10^{-12}$ and otherwise returns the current center. The fallback is unused in all 256 conditions, where $\|\widehat{g}\| \in [0.881, 1.388]$. Reusing the recovery output, it evaluates the thirteen prescribed physical step lengths with paired line-search noise. Its per-condition recovery-plus-step cost remains $8d + 13$ endpoints and two rounds. The diagnostic adds 3,328 step evaluations across the cohort. It changes only the norm entering the step grid, not the angular error or the recovery-query geometry.

I.5 Direction accuracy and downstream loss are separate outcomes

Forty thousand paired seed resamples provide percentile intervals with Bonferroni correction across the original 64-contrast family: two controls (robust Reverse and ZO-RankSGD), two outcomes, and sixteen task–radius–noise cells. These are ratios of arithmetic means, not means of per-seed ratios. Repeated radii and noise levels do not create new independent units. The comparison counts appear in Table 6.

Table 6: Non-even logistic direction and task comparisons. Counts give task–radius–noise cells whose Bonferroni-adjusted 95% ratio intervals favor robust Full. They are not success probabilities on new tasks.

Robust Full compared with	Direction MSE intervals below one	Task-loss intervals below one
ZO-RankSGD	16 / 16	8 / 16
Robust Reverse	6 / 16	2 / 16

With matched recovery endpoints, the robust Full/Reverse results provide limited evidence of a local-step benefit. The remaining intervals do not establish equivalence. `logistic_all_64_contrasts.csv` supplies every ratio and its marginal and adjusted interval. `logistic_`

`absolute_results.csv` gives all 64 task–radius–noise–method summaries, including absolute MSE and training/test loss. All 1,024 individual outputs are retained in `logistic_all_outputs.csv`.

The unit-normalized ZO-RankSGD control forms a separate diagnostic family of sixteen task-loss contrasts. Using 40,000 paired seed resamples, Bonferroni-adjusted intervals favor robust Full in $8/16$ cells, none favors the control, and all sixteen point ratios are below one. The same eight cells remain below one under the 64-comparison threshold as a conservative sensitivity check, not a joint old-plus-new family. Positive normalization preserves direction MSE exactly and improves the pooled Blood regularized training objective from 0.52057 to 0.51343, while robust Full still has the lower objective (Table 7). Estimator and recovery-query differences remain after this norm control.

Table 7: Physical-step control for ZO-RankSGD. The first three result columns give arithmetic mean post-step regularized training objectives F over 128 matched conditions per task. The last gives the robust Full/unit-normalized ZO-RankSGD ratio. All 3,328 new candidates pass a 192-bit interval audit. The maximum clean-score discrepancy upper bound is 2.45×10^{-16}.

Task	Robust Full	ZO-RankSGD	Unit-normalized ZO-RankSGD	Robust Full / unit-normalized
Blood	0.48848	0.52057	0.51343	0.9514
Banknote	0.36632	0.38180	0.38322	0.9559

J Validity Tests under Odd Remainders and Score Noise

The cubic experiment isolates invalid retention. Separate calibrated cohorts test shared-error recovery, smooth-radius calibration, and paid observable initialization. Non-even logistic recovery and supplementary local-step controls are evaluated in Appendix I.

J.1 Odd remainders: containment, coverage, and history

J.1.1 Protocol and retention policies

This branch reuses the 96 independent target–axis units in Appendix G.1, with 32 at each $d \in \{3, 8, 20\}$. It crosses $N/d \in \{8, 32\}$ with $\mu \in \{0, 0.003, 0.03, 0.3\}$, giving 768 conditions, each evaluated under four policies. Together with the 2,688 quadratic and 576 quartic conditions, the shared structural cohort comprises 4,032 conditions and 6,336 policy branches, not additional independent targets. All planned denominators are retained, including the 337 empty retained models.

The odd family uses Equation (33) with $E(x) = \|x\|^2/2$. Large shell evaluates all N endpoints at radius one. Small shell evaluates them at radius $1/8$. Retained evaluates the first $N/2$ endpoints at radius one and the remaining $N/2$ at radius $1/8$, then fits their complete cumulative ranking. Restart uses the same two batches and pays the same N evaluations, but its final fit retains only the second batch's $N/2$ endpoints. Both two-round designs use uniform directions. They isolate the effect of retained observations, not an adaptive query-width policy. In particular, the single-shell shifted-direction order is independently checked on every saved odd design rather than assumed from ideal normalization.

J.1.2 Diagnosing an empty retained model

To distinguish a solver failure from model inconsistency, reconstruct pure-gradient rows $a_i^\top v \geq 0$ implied by the observed ranking. A nonnegative dependence satisfies $\sum_i w_i a_i = 0$, $w_i \geq 0$, and $\sum_i w_i = 1$. Every feasible v must then satisfy $a_i^\top v = 0$ for all positive-weight rows. If those rows span $\mathbb{R}^d$, only $v = 0$ is possible, so the direction set is empty even under the weak closed model.

For all 337 empty retained models, an independent checker reconstructs the original implied rows and verifies nonnegative weights, exact cancellation, and full positive-support rank. These certificates establish nonzero-gradient impossibility, not merely failure to find a strict interior.

Table 8: Odd-remainder recovery diagnostics. Each cell gives true-direction feasibility/coverage counts out of 32 planned targets. Coverage counts only returned certificates; empty direction sets count as neither feasible nor covered. Restart pays N endpoints but retains only $N/2$.

d	N/d	μ	Large shell	Small shell	Retained	Restart
3	8	0	32 / 32	32 / 32	32 / 32	32 / 32
3	8	0.003	32 / 32	32 / 32	32 / 32	32 / 32
3	8	0.03	10 / 22	32 / 32	23 / 27	32 / 32
3	8	0.3	0 / 0	29 / 31	0 / 0	32 / 32
3	32	0	32 / 32	32 / 32	32 / 32	32 / 32
3	32	0.003	5 / 9	32 / 32	21 / 28	32 / 32
3	32	0.03	0 / 0	22 / 31	0 / 0	30 / 32
3	32	0.3	0 / 0	2 / 3	0 / 0	16 / 28
8	8	0	32 / 32	32 / 32	32 / 32	32 / 32
8	8	0.003	10 / 32	32 / 32	21 / 32	32 / 32
8	8	0.03	0 / 29	30 / 32	2 / 30	32 / 32
8	8	0.3	0 / 0	4 / 32	0 / 0	24 / 32
8	32	0	32 / 32	32 / 32	32 / 32	32 / 32
8	32	0.003	0 / 7	24 / 32	0 / 19	29 / 32
8	32	0.03	0 / 0	1 / 32	0 / 0	13 / 32
8	32	0.3	0 / 0	0 / 1	0 / 0	0 / 31
20	8	0	32 / 32	32 / 32	32 / 32	32 / 32
20	8	0.003	0 / 32	30 / 32	11 / 32	31 / 32
20	8	0.03	0 / 27	11 / 32	0 / 16	23 / 32
20	8	0.3	0 / 0	0 / 32	0 / 0	5 / 32
20	32	0	32 / 32	32 / 32	32 / 32	32 / 32
20	32	0.003	0 / 0	8 / 32	0 / 0	21 / 32
20	32	0.03	0 / 0	0 / 32	0 / 0	0 / 32
20	32	0.3	0 / 0	0 / 0	0 / 0	0 / 32

J.1.3 Containment, coverage, and retained history

All 2,304 single-shell branches, including Restart's retained small batch, have the same exact ranking as the corresponding shifted-gradient even instance. Its direction is feasible and covered in every branch. These are consistency and coverage checks. They do not imply that finite rankings uniquely determine that direction. The true gradient direction at the center is the normalized stored u and is assessed separately in Table 8.

A certificate encloses the fitted model. It can cover the true direction even after the model has excluded it, because the outer bound may be loose. Table 8 shows why containment and coverage require separate diagnostics. On a fixed shell, more observations can expose model mismatch by narrowing the feasible set around a biased direction. Restart keeps fewer constraints than Small shell, so its higher containment or coverage count does not establish better precision.

Of 768 retained conditions, 302 admit the true direction and 466 exclude it. Every exclusion is already present in the first batch. In 274 of those 466, the new small batch alone admits the true direction, yet keeping the old constraints prevents its re-entry (Table 9). Of the 466, 337 have no feasible nonzero gradient at all. The remaining 129 return another direction. Thus reducing the new shell's cubic bias and restoring the retained model's validity are distinct operations.

J.2 Matched error-contract experiments

This study uses 96 independent targets, with 32 at each $d = 3, 8, 20$. Targets, odd axes, and stored noise are reused across $N/d = 16, 32$ and three perturbations. This design gives 576 matched conditions. Each condition gives a first fit at $N/2$ and a cumulative fit at N endpoints. Solver parameters are identical throughout. Target, query, and noise seeds are in the companion manifest.

Table 9: True-direction exclusion under retained history. Each odd-remainder coefficient has 192 conditions (96 targets, two budgets). Membership columns record (first batch, new batch, retained model), with 1 denoting inclusion; the three patterns exhaust the data. The final column counts independently certified empty retained sets, a subset of the two true-direction exclusion patterns.

μ	$(1,1,1)$	$(0,1,0)$	$(0,0,0)$	Empty retained set
0	192	0	0	0
0.003	85	92	15	43
0.03	25	105	62	105
0.3	0	77	115	189
Total	302	274	192	337

The objective and stored observations are

$$f(x) = u^\top x + \|x\|^2/2 + \mu(q^\top x)\,\|x\|^2, \qquad y(x) = f(x) + \xi(x),$$

where u is a normalized Gaussian vector, q is a normalized orthogonalized Gaussian vector, and each endpoint error is uniform on $[-\nu, \nu]$. The three (μ, ν) settings are odd-only $(0.003, 0)$, noise-only $(0, 0.0003)$, and combined $(0.003, 0.00001)$. The combined setting uses both error sources but a lower noise amplitude than the noise-only setting, so the comparison is a sensitivity check rather than a factorial decomposition. A stored endpoint retains its original error. The first d unsigned queries are the standard axes, and the rest are uniform spherical draws. The first half use physical radius one. The second half use radius $1/8$ for odd-only and combined conditions, and radius one for noise-only conditions. Every axis and antipode counts toward the budget.

The decoder receives coordinates, integer ranks, and public budgets

$$\omega_i = \frac{\mu\,\overline{\|x_i\|}^{\,3} + \nu + 10^{-12}}{0.99},$$

rounded outward, where $\overline{\|x_i\|}$ is a checked upper norm bound. The supplied gradient lower bound is 0.99. The small numerical allowance covers the stored normalizations. It is not adjusted using the realized projection on q. Exact binary-rational polynomial scores plus stored errors determine the order. Objective parameters and cardinal scores enter only the evaluator and audits. The second fit retains the same chart and each endpoint's error budget.

An independent rational checker reconstructs observations, verifies every Full shared-error inequality and true physical-score witness, and recomputes supports and caps. True-direction membership in the zero-error model is checked independently on the same endpoints and ranks, isolating the model rather than acquisition.

Retained/first MSE ratios compare N with $N/2$ endpoints, not equal budgets. Marginal 95% percentile intervals use 20,000 paired target resamples, retaining pairing across budgets and perturbations within each dimension.

All 1,152 fits across the 576 conditions converge and are feasible; all caps cover the true direction. The zero-error model excludes the true direction in 333 final conditions (Table 10). Every marginal refinement interval lies below one, and the largest chart-envelope inflation is 1.047994, below the factor two allowed by the theory. Caps shrink in 574/576 conditions. Outer radii about changing centers need not be monotone even for nested sets.

J.3 A NON-EVEN SMOOTH OBJECTIVE WITH A PUBLIC RADIUS

To test Corollary 9, use the strongly convex shifted quartic

$$f(x) = u_0^\top x + \|x\|^2/2 + 0.01\sum_{j=1}^{d}(z_j + x_j)^4, \qquad \|u_0\| = 1, \quad z_j \in [-1, 1].$$

Its actual gradient is $g = u_0 + 0.04z^{\odot 3}$, not u_0, and its odd remainder is $0.04\sum_j z_j x_j^3$. On the unit ball, the gradient is 1.48-Lipschitz and $\|g\| \geq 1 - 0.04\sqrt{d} > 0.8$ for $d \leq 20$. Supply $L = 1.5$,

Table 10: Shared-error recovery. Each row uses 32 independent targets. Error settings are Odd $(\mu, \nu) = (0.003, 0)$, Noise $(0, 0.0003)$, and Combined $(0.003, 0.00001)$. Combined uses less noise than Noise. All robust fits are feasible, and all caps cover the true direction. "Excluded" counts true-direction exclusions by the zero-error model on the same final observations. MSE is the final mean squared angular error (rad^2). Ratios compare final N-endpoint with first-batch $N/2$-endpoint MSE. Brackets give marginal paired 95% percentile confidence intervals (CIs). Cap radii are final medians in radians.

d	N/d	Error	Excluded	MSE	Ratio [95% CI]	Median cap
3	16	Odd	$3/32$	1.30×10^{-4}	$0.158\ [0.0883, 0.291]$	0.0359
3	16	Noise	$2/32$	6.35×10^{-5}	$0.0814\ [0.0516, 0.130]$	0.0173
3	16	Combined	$3/32$	1.30×10^{-4}	$0.158\ [0.0886, 0.291]$	0.0361
3	32	Odd	$11/32$	1.90×10^{-5}	$0.180\ [0.0845, 0.382]$	0.0113
3	32	Noise	$3/32$	3.43×10^{-6}	$0.0540\ [0.0225, 0.117]$	0.00490
3	32	Combined	$11/32$	1.90×10^{-5}	$0.180\ [0.0845, 0.383]$	0.0114
8	16	Odd	$17/32$	4.78×10^{-5}	$0.229\ [0.182, 0.295]$	0.0347
8	16	Noise	$7/32$	7.37×10^{-6}	$0.0431\ [0.0297, 0.0626]$	0.0149
8	16	Combined	$17/32$	4.75×10^{-5}	$0.228\ [0.181, 0.294]$	0.0350
8	32	Odd	$31/32$	6.11×10^{-6}	$0.238\ [0.176, 0.315]$	0.0123
8	32	Noise	$15/32$	6.76×10^{-7}	$0.0917\ [0.0600, 0.142]$	0.00628
8	32	Combined	$31/32$	5.80×10^{-6}	$0.227\ [0.169, 0.296]$	0.0132
20	16	Odd	$31/32$	1.54×10^{-5}	$0.255\ [0.210, 0.312]$	0.0338
20	16	Noise	$24/32$	2.22×10^{-6}	$0.0646\ [0.0519, 0.0806]$	0.0163
20	16	Combined	$31/32$	1.47×10^{-5}	$0.243\ [0.202, 0.295]$	0.0370
20	32	Odd	$32/32$	1.30×10^{-6}	$0.0760\ [0.0659, 0.0870]$	0.00889
20	32	Noise	$32/32$	2.77×10^{-7}	$0.125\ [0.102, 0.155]$	0.00869
20	32	Combined	$32/32$	1.43×10^{-6}	$0.0834\ [0.0706, 0.0994]$	0.0118

$g_{\min} = 0.5$, and $a = 0.01 g_{\min}/(8L\sqrt{d})$. The divisor eight is an experimental choice, not a calibrated theorem constant.

Four independent (u_0, z) draws per $d = 3, 8, 20$ give 12 one-round conditions, each paying $32d$ endpoints including standard-axis pairs. After rescaling by a, the decoder receives coordinates, exact polynomial ranks, and outward-rounded budgets $La\,\|W_i\|^2/(2g_{\min})$. All fits meet the convergence threshold, and exact witness/support checks confirm true-direction retention and cap coverage. Caps range from 0.00409 to 0.00795 rad and point errors from 0.000355 to 0.003014 rad.

J.4 Observable initialization and retained recovery

The observable initializer constructs a shared-error chart from paid observations without a supplied direction cap. Its first batch has d coordinate pairs and $3d$ uniform pairs, for $8d$ endpoints. It uses the stronger axis bound and residual-checked refinements in Appendix F.5. All refinements are numerical. Failure to certify the factor-two criterion is reported without fitting.

The archived summary reports 116 conditions from 25 target units at $d = 8, 20, 50$. It partitions them into 68 conditions on thirteen units and 48 conditions on twelve additional units. The per-unit reconstruction of the 68-condition subset resides in the companion records and is not recoverable from the manuscript alone. Table 11 summarizes the independently enumerated 48-condition subset. All reported conditions complete under one common rule, with maximum chart inflation 1.99428. All 232 first- and second-batch fits converge and are feasible; every cap covers the true direction. A second batch adds $8d$ uniform endpoints at physical radius $1/8$, retaining the original chart and all prior constraints. Every final cap is tighter than its first cap. The manifest and `initialization_all_conditions.csv` retain the cohort identifiers.

The implementation stores physical coordinates $x_i = aW_i$ and physical budgets $B_i = \rho a^3$, with actual odd scores bounded by $0.99B_i$. Reducing the radius from one to $1/8$ therefore reduces stored budgets by $1/512$. Dividing coordinates and budgets by a gives the shell-normalized factor $1/64$. This synthetic continuation has no fixed-amplitude score-noise term, whose normalized allowance

Table 11: Observable robust initialization and retention. Four independent targets per dimension (twelve total) are reused across two error budgets $d\rho \in \{0.40, 0.55\}$ and two observation modes, giving sixteen conditions per row. Cap radii are medians in radians. The MSE ratio compares $16d$ with $8d$ endpoints, so budgets differ. All charts satisfy the factor-two criterion; every fit contains the true direction and every cap covers it.

d	Conditions	First cap	Final cap	Final / first MSE
8	16	0.6872	0.05834	0.03206
20	16	0.4927	0.05129	0.03786
50	16	0.3822	0.04092	0.02303

would instead grow as $\nu/(a\,\|g\|)$. The two observation modes use zero odd error or bounded shared odd error under the same public budget.

Continuation here jointly increases observations and decreases the physical radius. Its loss and cap changes do not isolate either intervention or establish an advantage over a matched final-only design. The finite success counts do not establish initialization throughout the full parameter region of Corollary 8.

J.5 Task-structured gradient calibration for noisy squared loss

On the standardized Airfoil and Concrete squared-loss tasks, set the unpenalized intercept to one and all feature coefficients to zero. Then

$$\partial_{\text{intercept}} F = 1 - \overline{y}_{\text{train}}.$$

Training-response centering supplies the public $g_{\min} = 0.99$ without revealing the full gradient. This is a center-specific metadata-derived bound, not a lower bound along an optimization trajectory. With physical radius $a = 1/512$, score-error bound $\nu = 10^{-4}$, and shell-normalized allowances $(\nu + 10^{-10})/(ag_{\min})$, all 64 initializations across 32 query/noise seeds on each task satisfy the factor-two criterion. The maximum inflation is 1.99547. Independent checks confirm retention and coverage in every robust fit.

These fixed-center initialization experiments are separate from the noiseless moving-center ridge trajectories in Section 4.3. A 192-bit interval audit of all 3,840 initial observations verifies the 10^{-10} numerical allowance, including coordinate-construction error. The maximum clean-score discrepancy upper bound is 4.76×10^{-16}. The audit also verifies every public intercept bound and shared-error inequality. The stored training responses give exact rational intercept derivatives $1 - \overline{y}_{\text{train}}$. `ridge_public_gradient_proof.json` contains these fractions and their comparison with 0.99. `ridge_initialization_conditions.csv` identifies all 64 conditions. `ridge_interval_checks.csv` gives the interval checks. `protocols.json` records query/noise seeds and the factor-two gate. Numerical chart refinements use no new oracle feedback. Their computation is recorded separately from the paid first batch and subsequent step evaluations.

K Computational Cost and Higher-Dimensional Recovery

We measure fitting, certification, independent checking, and memory on controlled one-round instances.

K.1 Stored constraints and numerical work

For $n \geq d$ physical pairs, the exact-even model has $p = d + n - 1$ variables after fixing the potential gauge and $2n - 1$ adjacent-ranking inequalities. Each dense QR Newton iteration costs $O(np^2)$ arithmetic operations and $O(np + p^2)$ storage. These per-iteration bounds exclude iteration counts and rational bit complexity. The shared-error chart has $p = d + 2n - 1$, the same ranking rows, and linear-size coordinate/error boxes, with the same dense-factorization order.

The gradient certificate initially forms at most n^2 Mirror/Reverse rows, using $O(n^2 d)$ storage. Zero-error transitive reduction preserves their implications. Reachability uses $O(n^2)$ additional storage

and $O(n^3)$ Boolean/dense arithmetic. The implementation solves $2d + 1$ support objectives with $d - 1$ section variables. Shared-error certificates explicitly retain their allowances without zero-error reduction.

Barrier-based sparse dual proposals are accepted only with nonnegative multipliers and the exact residual allowance in Equation (35). Singular or unsuccessful proposals are discarded. Proposal optimality is unnecessary. The crossover recipe is retained in the companion implementation notes.

K.2 A CONTROLLED DIMENSION–BUDGET STUDY

Twelve independent targets, four at each $d = 20, 50, 100$, use matched one-round budgets $N/d = 8, 16$. Independent normalized Gaussians give u, z in Equation (47), with $\lambda = 10^{-3}$. Uniform unit-shell antipodal queries use nested budget prefixes. All 24 conditions use the same exact ordering, float64 QR fit, dual crossover, rational supports, and independent tangent completion.

Each worker uses one allocated logical CPU and one shared A100 80-GB GPU. In Table 12, CUDA-synchronized certificate time includes dual proposals and rational checks. Separate recheck time includes independent verification and tangent completion. GPU allocation excludes cached reserved memory. Peak host resident memory, including Python/CUDA, is at most 1.27 GiB. These timings characterize shared hardware, not isolated-device throughput.

Table 12: One-round computation and recovery. Rows use four independent targets; times are medians in seconds. GPU denotes peak allocation in MiB. All 24 fits are exactly feasible; all caps cover the true direction.

$(d, N/d)$	Fit	Certify	Recheck	GPU	Cap range (rad)
$(20, 8)$	0.55	6.57	0.33	17.4	$[0.0380, 0.0408]$
$(20, 16)$	0.54	6.47	0.50	21.2	$[0.00664, 0.00916]$
$(50, 8)$	0.70	25.86	4.14	50.9	$[0.0214, 0.0261]$
$(50, 16)$	0.80	27.86	6.88	177.2	$[0.00521, 0.00584]$
$(100, 8)$	1.16	119.43	29.04	329.7	$[0.0162, 0.0179]$
$(100, 16)$	1.64	142.55	51.36	1287.7	$[0.00391, 0.00429]$

Table 12 shows that certification and independent checking dominate fitting. Larger budgets tighten caps but increase GPU workspace. At $d = 100, N = 1600$, about 640,000 Mirror/Reverse rows reduce to 836–849.

Evaluation cost and feedback latency. With P parallel workers, n_r paid endpoints in round r, endpoint time t_{eval} and feedback latency t_{fb}, an illustrative total time is $\sum_r \lceil n_r/P \rceil t_{\mathrm{eval}} + R t_{\mathrm{fb}} + T_{\mathrm{sort}} + T_{\mathrm{decode}}$. Thus $N = \sum_r n_r$ and R describe different resources, neither of which includes sorting or decoding.